Condensate Retention Effects on the Air-Side Heat Transfer Performance of Plain and Wavy-Louvered Heat Exchangers

J. Yin and A. M. Jacobi

ACRC TR-158 January 2000

For additional information:

Air Conditioning and Refrigeration Center
University of Illinois
Mechanical & Industrial Engineering Dept.
1206 West Green Street
Urbana, IL 61801

(217) 333-3115

Prepared as part of ACRC Project 91
Water Retention and Shedding
Effects on Air-Side Heat Transfer Behavior
A. M. Jacobi, Principal Investigator

The Air Conditioning and Refrigeration Center was founded in 1988 with a grant from the estate of Richard W. Kritzer, the founder of Peerless of America Inc. A State of Illinois Technology Challenge Grant helped build the laboratory facilities. The ACRC receives continuing support from the Richard W. Kritzer Endowment and the National Science Foundation. The following organizations have also become sponsors of the Center.

Arçelik A. S.
Amana Refrigeration, Inc.
Brazeway, Inc.
Carrier Corporation
Copeland Corporation
DaimlerChrysler Corporation
Delphi Harrison Thermal Systems
Frigidaire Company
General Electric Company
Hill PHOENIX
Honeywell, Inc.
Hussmann Corporation
Hydro Aluminum Adrian, Inc.
Indiana Tube Corporation
Lennox International, Inc.
Modine Manufacturing Co.
Parker Hannifin Corporation
Peerless of America, Inc.
The Trane Company
Thermo King Corporation
Visteon Automotive Systems
Whirlpool Corporation
Wolverine Tube, Inc.
York International, Inc.

For additional information:

Air Conditioning & Refrigeration Center
Mechanical & Industrial Engineering Dept.
University of Illinois
1206 West Green Street
Urbana IL 61801

217 333 3115

Abstract

The effect of condensation on air-side heat transfer performance has been studied for plain-fin-and-tube and wavy-louvered heat exchangers with fin spacings of 2.12, 1.57, and 1.27 mm. Wet and dry heat exchanger experiments have been conducted to obtain sensible heat transfer, pressure drop, and condensate retention data to help understand the effects of retained condensate on heat exchanger performance. Condensate retention behavior was characterized by measurements of the real-time and steady-state mass of retained condensate. Sensible j and friction factor correlations have been developed using dimensional analysis and the experimental data for the heat exchangers under wet and dry conditions. A condensate retention model has been developed to help predict the quantity of retained condensate on plain-fin-and-tube heat exchangers based on geometry, contact angles, and orientation.

Table of Contents

List of Figures

Page

Nomenclature

a	constant used in C.6
A	area (m^2)
A_{drop}	area of a droplet (cm^2)
A_{fr}	frontal area (m^2)
b	constant used in C.6
C	constant used in C.6
Cp	specific heat at constant pressure (kJ/kg-K)
D	diameter (m)
D_{coll}	collar outside diameter (m)
D_{AB}	binary mass diffusion coefficient (m^2/s)
D_{drop}	diameter of droplet (m), Equation 4.4
D_h	hydraulic diameter (m)
Ec	Eckert number
ΔP_{HX}	heat exchanger differential pressure (kPa)
f	friction factor
f_s	fin spacing (mm)
F_d	air drag force (N)
F_g	gravitational force (N)
F_s	surface tension force (N)
g	gravitational acceleration (9.81 m/s^2)
G	mass velocity based on minimum free flow area (kg/m^2-s)
h	enthalpy (kJ/kg)
h	air-side heat transfer coefficient (W/m^2-K)
h_i	coolant-side heat transfer coefficient (W/m^2-K)
h_l	height of slit used in A.21
H'	parameter defined in A.17
h_l	height of heat exchanger
j	sensible j factor
κ	thermal conductivity (W/m-K)

L fundamental dimension of length (see Appendix B)

length of heat exchanger in direction of air-flow

l width of condensate bridge (m) See Figure 4.2

L_f length of fin (m)

L_{max} maximum length of fin-tube bridge neglecting air-flow forces (m) See Figure 4.2

M dimension used in Figure A.2. fundamental dimension of mass (see Appendix A)

N_{tr} number of tube row in the direction of air-flow

N_t total number of tubes

Nu Nusselt number

P Plain (see Table 2.1)

Pr Prandtl number

Q heat transfer rate (KW)

r_i inner radius of circular fin (m)

R thermal resistance (K/W)

Rc coolant flow rate (pulse/s)

Re Reynolds number

S_s width of an enhanced zone (m) Table 4.1

St Stanton number

S_t transverse tube spacing (mm) (see Figure 2.5)

S_l longitudinal tube spacing (mm) (see Figure 2.5)

T temperature (^{o}C), fundamental dimension of temperature (see Appendix B)

t time (s), fundamental dimension of time (see Appendix B)

V velocity (m/s)

V_{bridge} volume of bridge (m^3), Equation 4.9

V_{drop} volume of droplet (m^3), Equation 4.4

W heat exchanger finned width (m)

WL wavy-louvered

Greek symbols

α angle of inclination (radians)

δ fin thickness (m)

Φ	fin efficiency
ϕ	relative humidity
γ	surface tension (mN/m)
η	surface effectiveness
Π	dimensionless group used in Appendix B
μ	dynamic viscosity (N-s/m^2)
θ	contact angle (radians)
θ_A	advancing contact angle (radians)
θ_M	mean contact angle (radians) $\theta_M=(\theta_A+\theta_R)/2$
θ_R	receding contact angle (radians)
ρ	density (kg/m^3)
σ	contraction ratio (A_{min}/A_{fr})

Subscripts

air	air
atm	atmospheric pressure (atm)
ave	average
c	coolant
cali	calibrated
coll	collar
corr	correlation
dp	dewpoint
dry	dry condition
f	fin
if	inner fin
equiv	equivalent
exp	experimental
in	inlet
it	inside tube
l	liquid

mair	mean air
min	minimum
max	maximum
out	outlet
read	reading
sens	sensible
scion	scion image
tot	total
wet	wet condition

Chapter 1 – Introduction and Literature Review

Introduction

Condensation will occur on a heat transfer surface when the surface operates below the dewpoint of the incoming air. Depending on the wettability of the heat exchanger surface, condensate will form in either a dropwise or filmwise mode and will continue to accumulate on the surface until it is removed by air-flow, gravitational, or surface tension forces. The effect of condensation on heat exchanger performance has been of interest to many researchers. Whether it is in air-conditioning or in refrigeration applications, the condensation that occurs on a heat exchanger surface will affect the pressure drop and heat transfer performance. Condensate retained on a heat exchanger will restrict air flow and increase the air-side pressure drop across the heat exchanger. Although there have been many studies of condensing heat exchangers and some initial efforts on understanding the physics of condensate retention, a good model for predicting the quantity of retained condensate has not been developed and the effects of condensation on heat exchanger performance are not clearly understood.

The purpose of this project was to determine the effect of condensate on air-side heat transfer performance and to develop a new model for predicting the quantity of retained condensate on a heat exchangers. A wind tunnel was designed and constructed for testing heat exchangers under dry and condensing conditions. Experiments were conducted to obtain steady-state and real-time measurements of condensate retention. Furthermore, heat transfer and pressure drop data for heat exchangers under dry and

condensing conditions were recorded. The data from the experiments were used to aid in development and validation of a retention model.

Literature Review

Early Studies

Bettanini [1] studied simultaneous heat and mass transfer on a simple planar surface mounted in a vertical orientation. Under wet conditions an increase in heat transfer for both filmwise and dropwise condensation was observed, but the dropwise condensation had a greater effect. The enhancement in heat transfer was explained by the increased surface roughness of the heat transfer surface when condensation forms. An analogous effect was obtained by increasing the surface roughness of the test surface by spraying solid gypsum drops on the plate. It was concluded that the increase in heat transfer performance depended on both the surface roughness and the mass transfer on heat transfer.

Guillory and McQuiston [2] studied a parallel-plate heat exchanger under condensing conditions. Experimental j and f factors for the heat exchanger under wet and dry conditions were compared. Results showed an increase in both pressure drop and heat transfer for the exchanger when operating under wet conditions. In agreement with Bettanini, Guillory and McQuiston explained that the condensate forming on the heat exchanger increased the surface roughness and increased the heat transfer and pressure drop under wet conditions.

Realizing that condensate was an important factor in heat transfer, McQuiston [3] extended his work to observe water retention behavior in his parallel plate heat exchanger

studies. Again an increase in friction factor and heat transfer was found for exchangers under wet conditions. He also found that at low Reynolds numbers a considerable time was required for steady state droplet formation. At steady state a particular surface was found to hold a given amount of condensate over the range of Reynolds numbers tested. McQuiston made visual observations and found that dropwise condensation was promoted on aluminum, copper-nickel, and copper surfaces. The aluminum surface was found to retain the most condensate while copper held the least; however, the surface energy of the test surface, i.e., the contact angles, were not measured. It was observed that larger drops were associated with larger quantities of condensate.

Tree and Helmer [4] also studied a parallel plate heat exchanger under condensing conditions. Unlike Guillory and Mcquiston, they found that condensation did not effect the sensible heat transfer and pressure drop for laminar air flow. However, agreement was found in the transitional and turbulent regime, where condensate was found to increase heat transfer and pressure drop.

Plain-Fin-and-Tube Heat Exchangers

Heat transfer for plain-fin-tube heat exchangers exposed to condensing conditions were studied by McQuiston [5]. He tested five heat exchangers with fin spacings of 6.35, 3.18, 2.54, 2.12, and 1.81 mm and developed correlations for both wet and dry conditions [6]. Three surface conditions were studied: dry surface, wet surface with filmwise condensation, and wet surface with dropwise condensation. It was found that the type and condition of a surface has a significant effect on the heat, mass, and momentum transport processes. It was noted that there were two modes of condensation, but the contact angles

were never measured. Under condensing conditions McQuiston found an increase in sensible heat transfer for heat exchangers with a fin spacing of 6.35 and 3.18 mm. However, for heat exchangers with a fin spacing less than3.18 mm, wet surface conditions showed a decrease in sensible j. At wider fin spacings, the effect of filmwise condensation is minor while dropwise condensation will increase the friction factor significantly.

Seshimo *et al.* [7] conducted an experimental study of the air-side performance of a single-row plain-fin-and-tube heat exchanger under condensing conditions. It was found that, under wet conditions, there was an enhancement in heat transfer and an increase in pressure drop. Heat transfer increased about 20% and the pressure drop increased by 30 to 40%. This behavior was attributed to the presence of condensate on the heat exchangers.

Wang *et al.* [8] studied the performance of plain-fin-and-tube heat exchangers under dehumidifying conditions. The effects of fin spacing, number of tube rows, and inlet conditions were investigated. Nine plain-fin-and tube heat exchangers were tested with fin spacing ranging from 1.82 mm to 3.2 mm and 2, 4, and 6 tube rows. Heat transfer performance and friction factors were observed for the exchangers at a relative humidity of 50% and 90%. The friction factors for wet coils were found to be much larger than those of dry coils. For fully wet conditions, the friction factors were found to be 60 to 120% higher than for dry conditions and insensitive to change in inlet air relative humidity, fin spacing, and the number of tube rows. Sensible j factors under dehumidifying conditions were not found to be dependent on the inlet air conditions. Under wet conditions, a degradation in sensible heat transfer was seen at low Reynolds numbers. At high Reynolds numbers a small enhancement in heat transfer performance

was observed under wet conditions but the enhancement disappeared as the number of tube rows increased.

Korte and Jacobi [9] studied the effects of condensate retention on the air-side performance of plain-fin-and-tube heat exchangers. Experiments were conducted under dry conditions and then repeated under condensing conditions. It was found that the heat transfer performance under condensing conditions was dependent on the fin spacing. An enhancement in heat transfer for wet conditions was seen for a heat exchanger with a fin spacing of 6.35 mm but not for a heat exchanger with a fin spacing of 3.18 mm. The results for the heat exchanger with a fin spacing of 3.18 mm showed the heat transfer performance under wet conditions to sometimes be better and sometimes worse than for dry conditions. It was also found that the effect of condensation on friction factor was dependent on fin spacing. Similar friction factors were observed for a heat exchanger with a fin spacing of 6.35 mm under wet and dry conditions. At a fin spacing of 3.18 mm, there was a significant increase in friction factor under wet conditions. However, with increasing air-flow rates the quantity of retained condensate and the increase in friction factor decreased.

Chuah *et al.* [10] performed experiments on the dehumidification performance of a finned tube air-to-water heat exchanger. Experiments were conducted to measure the heat and mass transfer performance at various air velocities and water flow rates. It was found that the dehumidification capacity increased with the water velocity, but decreased with increasing air velocity, except at the highest water velocity. For increases in dehumidification performance, increases in water velocity was necessary. Experimental data were compared to published correlations and the calculated dehumidification

capacity was overpredicted by as much as 1.5 to 2 times at the maximum air velocity. Discrepancies were attributed to differences in heat exchanger geometry and revised correlations were developed.

Ha *et al.* [11] studied the hydraulic performance of wet fin-and-tube heat exchangers with various wettability surfaces. Contact angle measurements were obtained and used to characterize each of the different surfaces. For all surfaces, an increase in pressure drop was found for heat exchangers under wet conditions. The increase in pressure drop was greater with increasing contact angles. It was also found that surfaces with smaller contact angles held less condensate and required less time to reach a steady value of retained condensate. Furthermore, pressure drop models for dry and wet heat exchangers with dropwise condensation were developed.

Enhanced-Fin Heat Exchangers

Yoshii *et al.* [12] examined the effects of dropwise condensation on the pressure drop and heat transfer performance of wavy fin heat exchangers. It was found that pressure drop for wet heat exchangers was 50 to 100% higher than for dry exchangers. Under wet conditions, a 20 to 40% enhancement in heat transfer coefficient was found for heat exchangers. In order to investigate the effect of condensate on heat transfer and flow loss, flow patterns were visually studied in a water tunnel with simulated condensate on fin surfaces. Various condensate geometries were studied and it was concluded that condensate on wet surfaces had complicated effects on heat transfer and flow loss. Some drops were found to increase the heat transfer coefficient under wet conditions while

others drops decreased or had no effect on the heat transfer coefficient for the fin configuration tested.

Mirth and Ramadhyani [13] conducted an experimental study of wavy-finned heat exchangers to determine the heat transfer performance under wet and dry conditions and to develop dry-surface Nusselt number and friction factor correlations [14]. The effect of condensation on Nusselt numbers was inconclusive with wet results scattered among the dry results. Similar to other heat exchanger studies [5] [7], the friction factor was found to be greater under condensing conditions when compared to dry conditions.

Youn *et al.* [15] studied the pressure drop and heat transfer characteristics of plain, wavy and wavy-slit fin-and-tube heat exchangers under dry conditions. Under dry conditions, plain-fin-and-tube heat exchangers were found to have friction factors 20 to 45% lower than that of the wavy-fin geometry at the same Reynolds number. It was also shown that the heat transfer coefficient for a wavy-fin heat exchanger is higher than for a plain-fin exchanger. The difference in heat transfer between plain-fin and wavy-fin exchangers becomes larger at higher air velocities and larger fin spacings.

Modeling Condensate Retention

Jacobi and Goldschmidt [16] proposed a simple condensate retention model that examined condensate bridges that formed between adjacent fins on a baffled, fin-tube heat exchanger. The sensible j factor for condensing heat exchangers was found to be higher than the dry case at high Reynolds numbers. However, at low Reynolds numbers the dry j factor was found to be higher than the wet case. The model was successful in explaining the cross-over that was noticed in this sensible j factor behavior.

Korte and Jacobi [9] developed a model to predict the quantity of retained condensate for uncoated aluminum plain-fin-and-tube heat exchangers with a fin spacing of 6.35 mm. The quantity of retained condensate was determined by calculating the volume of retained condensate and multiplying this volume by the density of the water. Unlike previous studies, the model incorporated advancing and receding contact angles that were used to determine surface tension forces. Modeling techniques were relatively successful in predicting the quantity of retained condensate for the heat exchanger with a fin spacing of 6.35 mm; however, many higher order effects that complicate drop distributions and the area covered by droplets were not included.

Objectives

The objectives of this project were to determine the effect of condensate retention on air-side heat transfer performance and to develop a condensate retention model for predicting the quantity of retained condensate on plain-fin-and-tube heat exchangers. Air-side heat transfer performance has been determined for heat exchangers under dry and condensing conditions. Experiments were conducted to obtain sensible heat transfer, condensate retention, and pressure drop data to help understand the effects of condensate on heat exchanger performance. A model has been developed to help predict the quantity of retained condensate on a heat exchanger surface based on geometry, contact angle, and orientation. The model considers the balance between gravitational, air-flow, and surface-tension forces on condensate droplets.

Chapter 2 - Experimental Apparatus and Methods

A closed-loop wind tunnel was designed and constructed for testing heat exchangers under condensing conditions. Heat exchanger performance and condensate retention measurements were obtained using the apparatus. This chapter describes the experimental apparatus, instruments, experimental procedures, and heat exchangers tested for this research.

Experimental Apparatus

The experimental apparatus consisted of a closed-loop wind tunnel, a test section for testing of heat exchangers exposed to horizontal air-flow, and a coolant loop which circulates a single-phase coolant. An electronic balance was used to measure the quantity of condensate retained on the heat exchanger surface in the wind tunnel, and a CCD camera was used to record images of water droplets used for contact-angle measurements. A closed environment "glove box" was used to study droplet distribution on a stock fin sample.

The wind tunnel is shown schematically in Figure 2.1. It was used to obtain measurements of retained condensate and heat-transfer performance for various types of heat exchanger geometries. Experiments were conducted with a horizontal flow of air, and specimens were tested at various air flow rates typical to refrigerator/freezer, room air-conditioning, and mobile air-conditioning applications. The closed-loop wind tunnel allowed temperature, humidity, and air flow rate control. Air temperature was controlled by varying the power supplied to five electical resistance heaters which were capable of

adding 2.5 kW to the air flow. Evenly spaced Type-T thermocouples were used both upsteam and downstream of the test section to measure the inlet and outlet air temperature. A six-thermocouple grid was used upstream and a twelve-thermocouple grid was used downstream to measure the average inlet and outlet air temperatures. Each thermocouple was individually referenced to a thermocouple located in an ice bath, and calibrated to a NIST traceable mercury-in-glass thermometer using a thermostatic bath. Calibration data were fit with fifth order polynomials for each thermocouple to give an uncertainty of ±0.3°C. The dewpoint of the air was maintained by injecting steam at a controlled rate. The dewpoints of the air were measured by chilled mirror hygrometers with a measurement uncertainty of ±0.2°C. The inlet dewpoint measurement was used to provide a control signal for closed-loop dewpoint control. The control signal was sent to a PID controller which adjusted the output of the humidifier to maintain the desired inlet air dewpoint. Both the heaters and the steam injection were located downstream of the test section before the axial fan. The axial fan mixed the conditioned air and provided volumetric flow rates up to 8.55 m^3/min. Air was drawn from a thermal mixing chamber and passed through a set of screens, honeycomb flow straighteners, and a 9:1 contraction to obtain steady laminar flow before passing through the test section.

A unique test section, shown in Figure 2.2, was designed for testing wet heat exchangers. The design allows for both real-time and steady-state measurements of the mass of retained condensate. The test section was constructed using clear acrylic to allow for optical access and insulated with 1.27 cm thick foam. An interchangeable frame was implemented to allow for testing of heat exchangers of varying length. Upstream and

downstream pressure taps were located on all four sides of the rectangular test section for measuring the pressure drop across the heat exchanger. The pressure taps were located approximately three inches upstream and downstream of the heat exchanger and on the centerline of each side of the test section. An electric manometer with an uncertainty of ±0.124 Pa was used to measure the air-side pressure drop across the heat exchanger. Face velocities were measured at the test section using a constant temperature thermal anemometer. The face velocity was determined by taking three equally spaced measurements traversing the height of the heat exchanger at each of the five velocity measurement locations shown in Figure 2.3. A total of fifteen measurements were recorded and an average face velocity was determined. The velocity measurements were within 13% of the average at the lowest velocity and 8% at the highest velocity. The maximum turbulence intensity, measured outside of the thermocouple wakes, was found to be 1.4%.

A single-phase ethylene glycol (DOWTHERM 4000) and water mixture was circulated on the tube side of the heat exchanger. A chiller controlled the coolant temperature, and the mixture was circulated through a copper tubing loop by two pumps. The copper tubing loop was insulated with 9.5 mm thick foam, (estimated foam conductivity of 0.3 W/mk). The heat exchanger was connected to the copper tubing with flexible, reinforced, PVC tubing which was also insulated by 9.5 mm thick foam. Coolant-side temperatures were measured using type-T immersion thermocouples located approximately two meters upstream and downstream of the heat exchanger. The thermocouple junction was installed at approximately the center of the copper tube and

before reaching the thermocouple, the glycol and water mixture passed through several elbows at Reynolds numbers greater than 6000. Each thermocouple was individually referenced to a thermocouple located in an ice bath. Coolant flow rate was measured using an oscillating piston type flow meter with a manufacturer reported measurement uncertainty of ±0.5%. A transmitter attached to the flow meter provided a 1-5V pulse with a frequency proportional to the volumetric flow rate. A Philips programmable timer/counter was used to count the number of pulses over a timed cycle with an uncertainty of ±2 pulses.

A glove box as shown schematically in Figure 2.4 was designed and constructed for studying droplet distribution on the fin surface. The apparatus was a sealed box made of clear plexiglas. Inside the closed environment was a Peltier device used for cooling a fin stock sample. A beaker of water was used to humidify the air in the glove box. Water was condensed onto the fin sample, and photographs were recorded at various locations of the fin.

Experimental Conditions and Procedures

For dry experiments a range of conditions were used to study heat transfer, air-side pressure drop, and condensate retention. Heat exchangers were exposed to an air velocity range of approximately 0.8 to 2.0 m/s. For dry experiments the inlet dewpoint of the air was kept at a minimum. In order to ensure that condensation did not occur during a dry experiment, the inlet coolant temperature was set so that the temperature of the tube wall was above the dewpoint of the air. Inlet temperatures were monitored to determine

when conditions had reached steady-state. Steady-state conditions were determined when the inlet air temperature varied by less than ±1°C and the inlet coolant temperature varied by less than ±0.2°C over a period of approximately 2 minutes. The thermocouples, chilled mirror hygrometers, and the coolant flow meter were connected to a computer data acquisition system. Eleven readings from each instrument were recorded over a period of 45 seconds, and the results for each instrument were averaged. While the data acquisition system acquired temperature and coolant flow-rate data, the pressure drop and face velocity measurements were recorded manually using an electronic manometer and constant-temperature anemometer. While recording the data the average inlet air temperature varied by less than ±0.15°C and the coolant inlet temperature varied by less than ±0.2°C.

For wet experiments a variety of test conditions were set to ensure condensation on the heat exchangers. Wet-experiment conditions were achieved by setting the inlet dewpoint to approximately 23.9°C, inlet air temperature to 34°C, and inlet coolant temperature to about 3°C. Similar to the dry experiments, the inlet air temperature and inlet air dewpoint were used to determine steady-state conditions. Steady-state conditions were satisfied when the inlet air temperature varied by less than ±1°C and inlet coolant and dewpoint varied by less than ±0.2°C over a period of approximately 2 minutes. However, unlike the dry experiments the inlet conditions were not the only determining factors for steady-state conditions. Under condensing conditions, sufficient time was allowed for retained condensate on the heat exchangers to reach steady-state. The minimum amount of time needed for condensate retention to reach a steady value was

determined from the real-time retention measurements. For experiments where real-time retention measurements were not recorded, heat exchangers were exposed to condensing conditions for a minimum of one hour before data were recorded.

Real-time measurements of retained condensate were obtained by placing the balance below the heat exchanger support. The weight of the heat exchanger and retained condensate was translated through the support onto the balance. The weight was measured using a calibrated electronic balance with readability of 0.1 g and recorded every 30 seconds until the retention reached a steady value. From the real-time measurements, condensate retention was found to reach a steady value within 20 minutes. The steady-state quantity of retained condensate was determined by exposing the heat exchanger to prolonged condensing conditions and then removing the heat exchanger loaded with condensate. The heat exchanger was weighed, allowed to dry, and then weighed again to determine the quantity of retained condensate. The real-time measurement for quantity of retained condensate measured in the test section agreed within 15% of the steady state value.

Heat Exchanger Specifications

This research project studied plain-fin-and-tube heat exchangers and wavy-louvered fin exchangers. Diagrams of the two types of heat exchangers are shown in Figures 2.5 and 2.6. Experiments conducted on these heat exchangers measured heat transfer performance under both wet and dry conditions. Furthermore, the amount of retained condensate for both real-time and steady-state conditions were studied. By obtaining such data, the effects of retained condensate on heat exchanger performance

could be studied. The plain-fin-and-tube heat exchangers were used as a baseline for comparison to the more complicated wavy-louvered fin exchangers. Figure 2.7 shows the details for the wavy-fin geometry used in this research. All heat exchangers had an uncoated fin surface. Heat exchanger specifications are noted in Table 2.1 and Table 2.2.

Contact Angle Measurements

Johnson and Dettre [17] discussed several methods for measuring advancing and receding contact angles. The advancing and receding contact angles are the significant angles that define retention characteristics. The maximum possible contact angle or advancing contact angle is established as the contact line advances over a previously unwetted portion of the solid. The receding contact angle is the minimum possible contact angle and is established as the contact line recedes over a previously wetted portion of a solid. For this research the technique that was adopted for measuring contact angles is shown in Figure 2.8 and involves the adding and removing of water through a syringe to a droplet laying on a horizontal surface. The syringe was held in contact with the droplet throughout the experiment and a CCD camera was used to take a digital photograph of the droplet at the onset of motion of the contact line. The advancing and receding contact angles were then measured using Scion Image, a scientific image acquisition and analysis software. The difference between these two angles provides the interfacial surface tension forces that allow for a droplet to stick to a surface. Measurements were recorded for a new stock fin surface along with samples of fin that were exposed to condensing conditions. These exposed samples were obtained by cutting the plain-fin-and-tube heat exchangers that were used for this research. The contact

angles for an unexposed fin surface and a surface exposed to condensing conditions is shown in Table 2.3.

Uncertainty

Details of uncertainties in the experimental measurements are discussed in Appendix C. The chilled mirror hygrometers used to measure the dewpoint of the air had a measurement uncertainty of ±0.2°C. Air-flow velocities were measured using a constant thermal anemometer and had a calibrated uncertainty of 1%. The electronic manometer used to measure the air-side pressure drop across a heat exchanger had an uncertainty of 0.124 Pa. Type-T thermocouples were used to measure the air and coolant temperatures and had a calibrated uncertainty of ±0.3°C. Coolant flow rate was measured with an oscillating piston type flow meter and had a measurement uncertainty of ±0.5%. The uncertainty in condensate retention measurements was hard to calculate since the uncertainties in the electronic balance are negligible to other sources of error. The values for the mass of retained condensate determined from the real-time experiments agreed within 15% of the steady-state values.

The propagation of error through the measured values introduces an uncertainty in calculated parameters. The uncertainty in coolant mass flow rate was determined to be 0.7%. The uncertainty in Reynolds number based on collar diameter was approximately 10% and the air-side heat transfer coefficient had an uncertainty of about 11%. The sensible j and friction factor had an uncertainty of 11.9% and 20.3%, respectively.

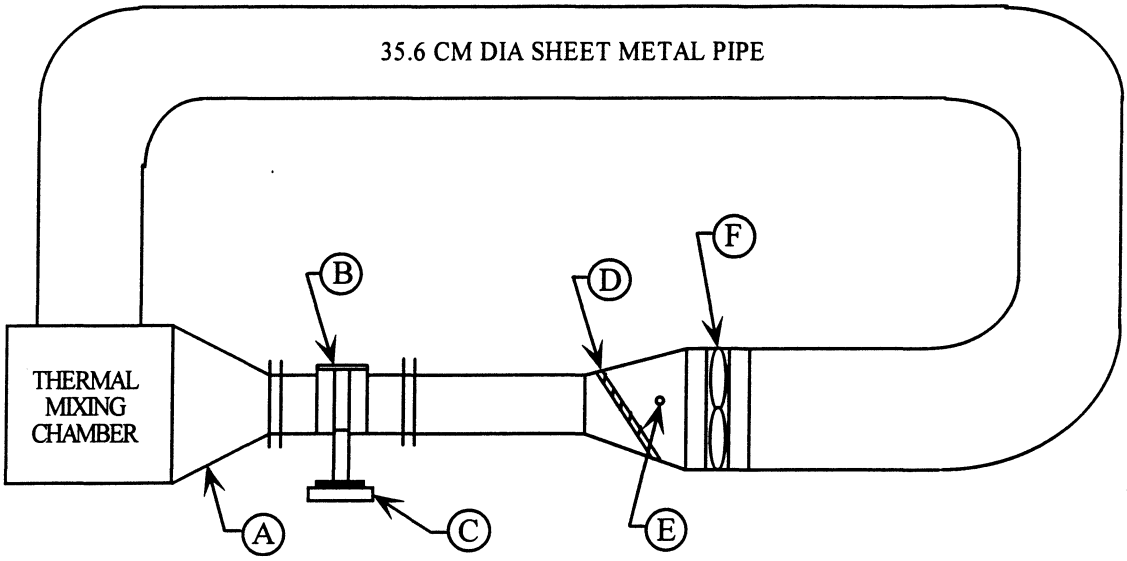

Figure 2.1 Wind tunnel for testing heat exchangers under condensing conditions and exposed to horizontal airflow (A) 9:1 contraction (B) insulated test section (C) calibrated electronic balance (D) five electrical resistance heaters, (E) steam injection (F) axial fan.

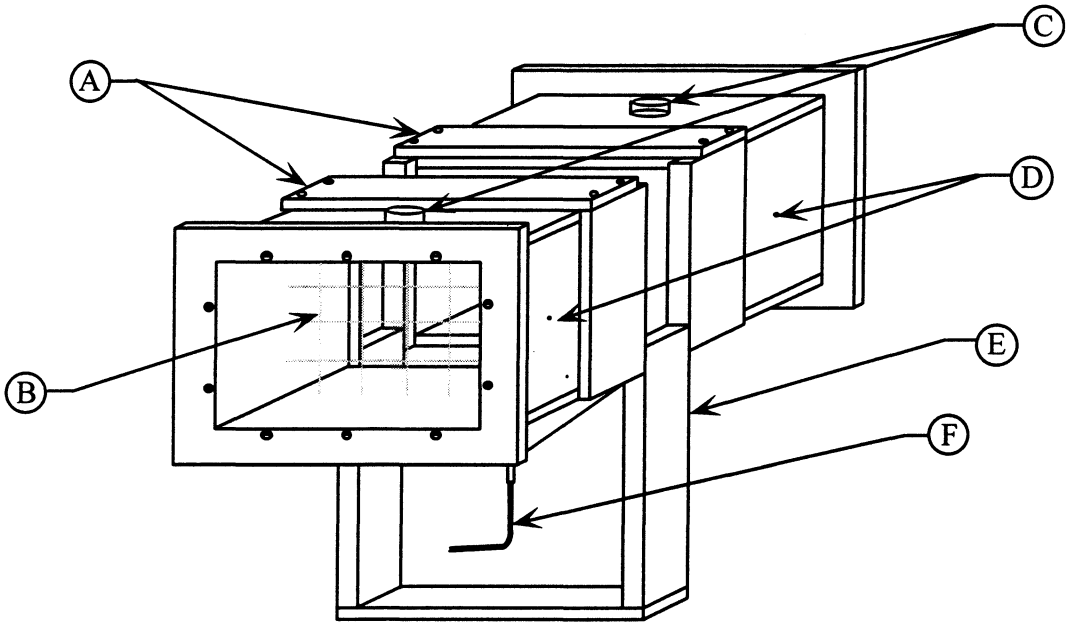

Figure 2.2 Test section used for testing of wet heat exchangers (A) interchangeable frame (B) thermocouple grid (C) chilled mirror hygrometers (D) pressure taps (E) heat exchanger support (F) funnel.

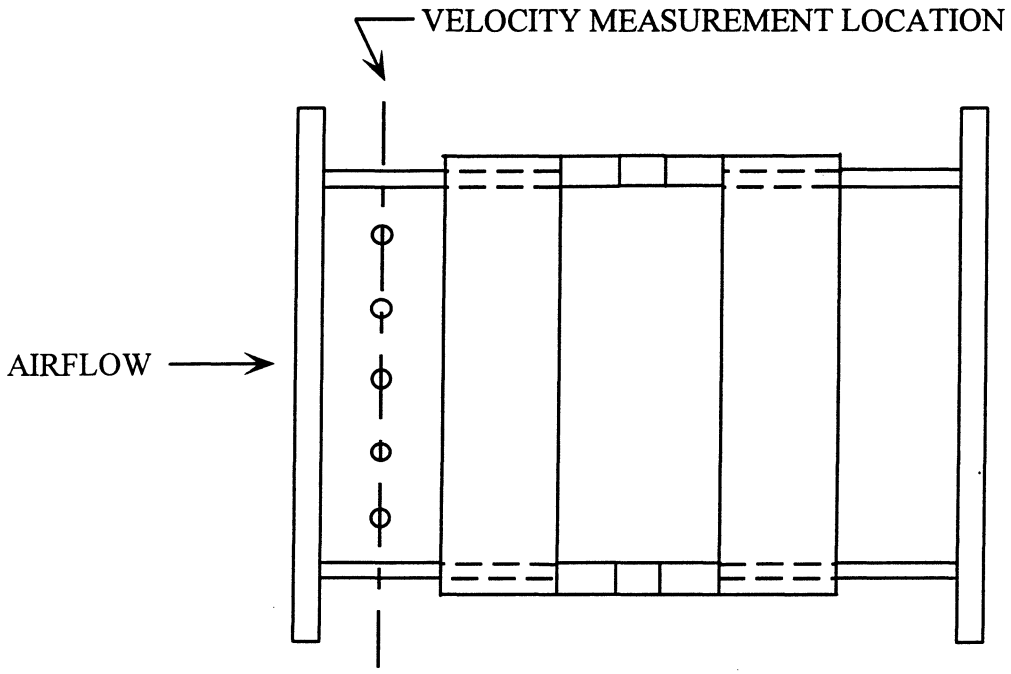

Figure 2.3 Top view of test section showing velocity measurement locations. At each measurement location three equally spaced velocity measurements traversed the height of the heat exchanger.

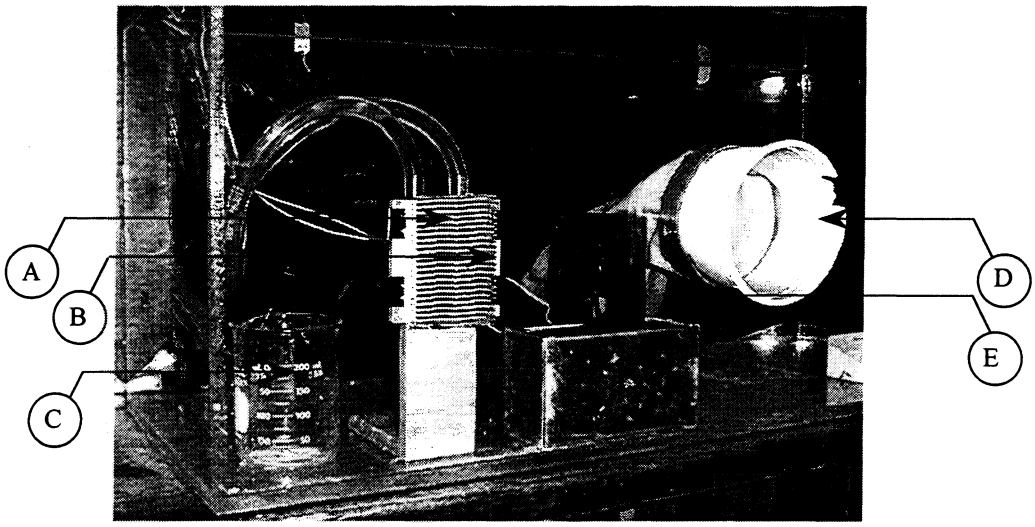

Figure 2.4 Closed environment glove box apparatus for examining condensing fin samples (A) peltier device and liquid heat exchanger (B) fin stock (C) beaker with water (D) glove (E) fan.

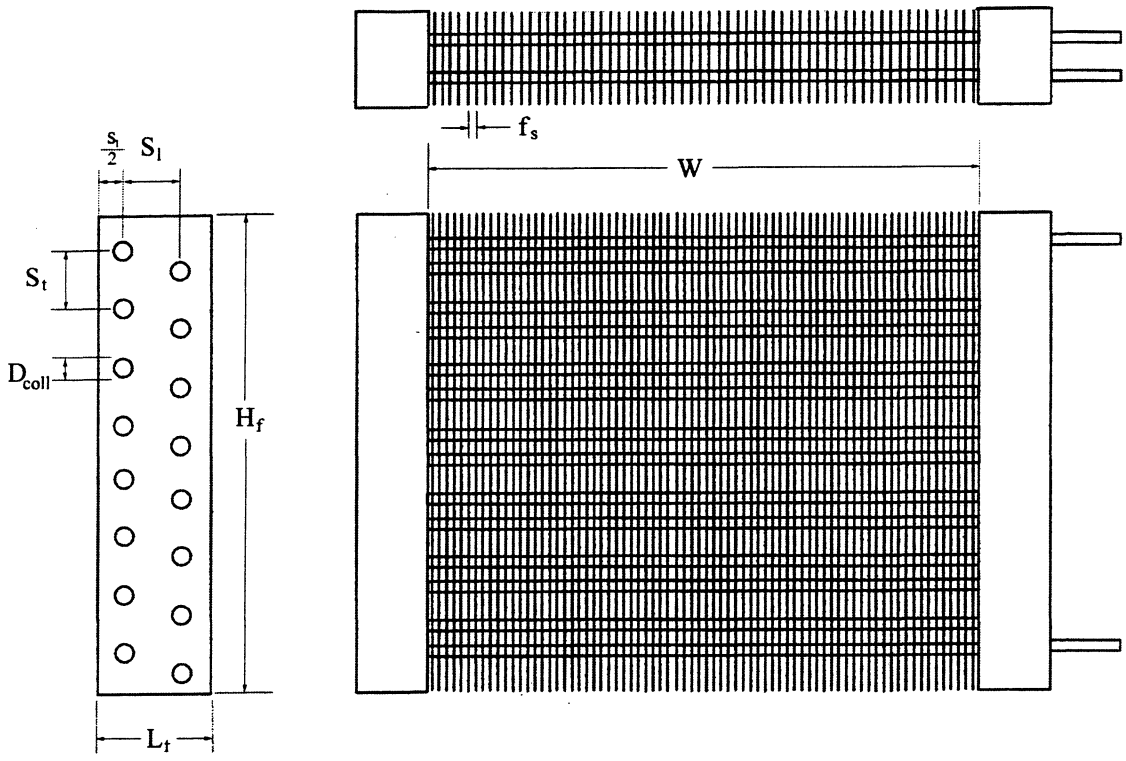

Figure 2.5 Heat exchanger geometry for plain-fin-and-tube heat exchangers.

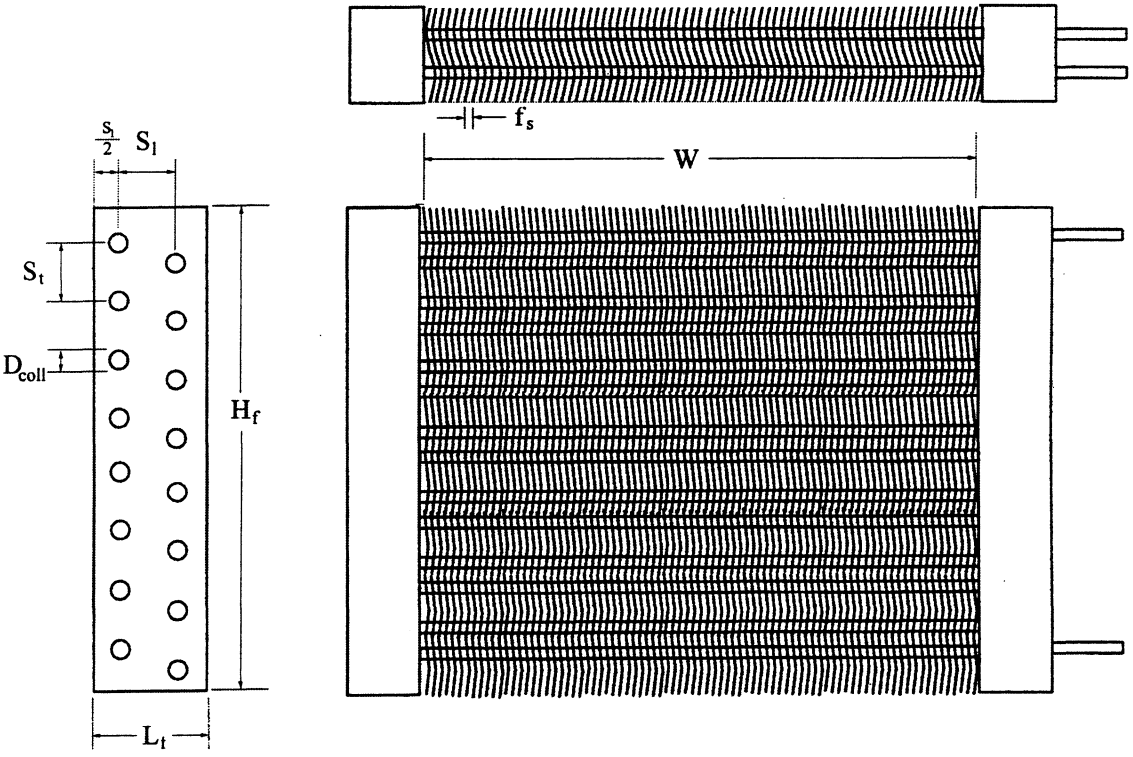

Figure 2.6 Heat exchanger geometry for wavy-louvered heat exchangers.

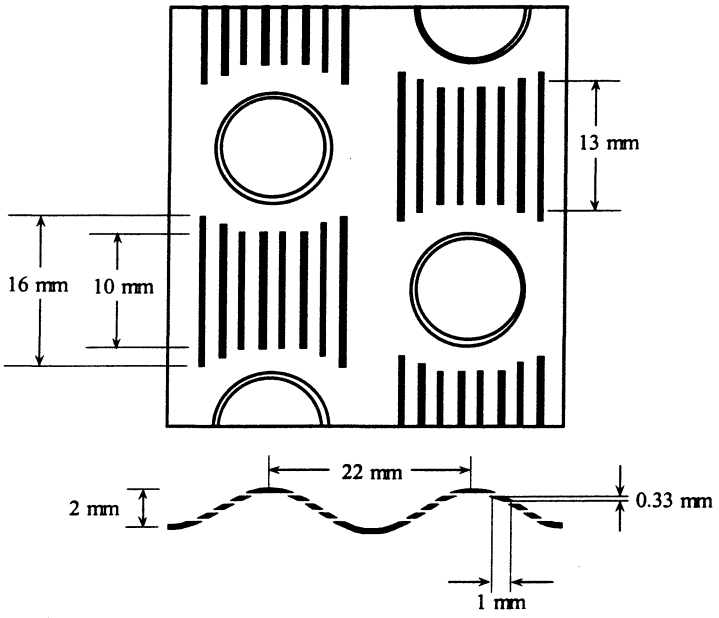

Figure 2.7 Details of wavy-louver fin geometry

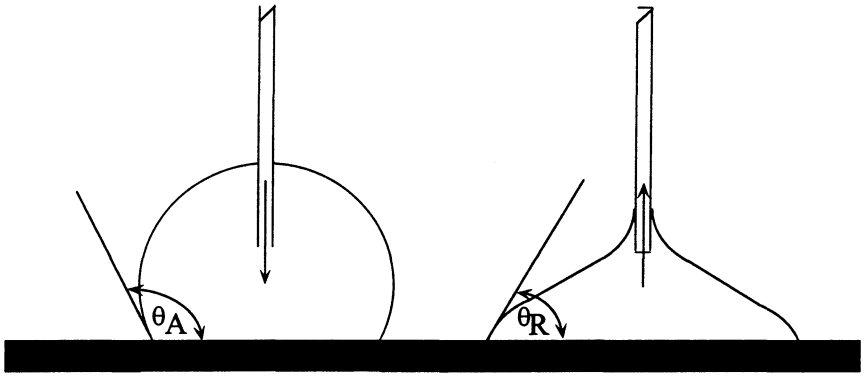

Figure 2.8 Technique for measuring contact angles which involved the adding and removing of water through a syringe to a droplet laying on a horizontal surface [17]

Table 2.1 General heat exchanger specifications

Heat Exchanger	**1.27P, 1.59P, 2.12P, 1.27PS, 1.59WL, 1.59WL, 2.12WL**
Number of Tubes	2 rows with 8 tubes in each row
W (mm)	304.8
H_f (mm)	203.2
L_f (mm)	44.1
S_t (mm)	25.4
S_l (mm)	22.0
δ (mm)	0.114
Fin Material	Aluminum
Tube Material	Copper

Table 2.2 Heat exchanger specifications

HX	**2.12P**	**1.59P**	**1.27P**	**2.12PS**	**2.12WL**	**1.59WL**	**1.27WL**
f_s (mm)	2.12	1.59	1.27	2.12	2.12	1.59	1.27
D_{coll} (mm)	9.65	9.65	9.65	7.11	9.65	9.65	9.65

Table 2.3 Contact angle measurements for new and exposed fin.

Material	**Condition**	**θ_A**	**2 σ Deviation**	**θ_R**	**2 σ Deviation**
Uncoated Aluminum	New	89.6°	1.2°	42.4°	3.0°
	Exposed	85.5°	11.0°	37.3°	18.6°

Chapter 3 - Experimental Results and Discussion

Real-Time Condensate Retention

A plot showing condensate retention versus time for the plain-fin-and-tube heat exchanger with a fin spacing of 2.12 mm over a range of face velocities is shown in Figure 3.1. Condensate accumulated on the heat exchanger and is held by surface tension forces. The condensate began to shed when air-flow and gravitational forces overcame the surface tension forces. The quantity of retained condensate increased and reached a maximum. Shortly after reaching the maximum, the quantity of retained condensate dropped. This drop in quantity of retained condensate means that the amount of condensate shedding off the heat exchanger is greater than that accumulating on the heat exchanger. This pronounced maximum behavior is seen at all face velocities for the plain fin heat exchanger with a fin spacing of 2.12 mm. Eventually the retention reaches a steady value, reflecting an equilibrium between condensate deposition and shedding. Real-time retention behavior for plain-fin-and-tube heat exchangers with fin spacings of 1.27, 1.59, and 2.12 mm exposed to approximately the same face velocity is shown in Figure 3.2. This figure shows that the pronounced maximum behavior disappears as the fin density increases.

As shown in Figure 3.3, condensate retention versus time for the wavy-louvered heat exchanger with a fin spacing of 1.59 mm did not exhibit the pronounced maximum observed on the lower fin density plain-fin heat exchangers. The plot shows that for a range of face velocites the retained condensate increased and approached a maximum. After reaching the maximum, the quantity retained was constant. As shown in Figure 3.4

the same behavior was observed for each of the different fin spacings for this type of heat exchanger.

Steady-State Condensate Retention

Steady-state condensate retention results are shown in Figures 3.5 and 3.6. Experiments were performed on all the heat exchangers except for the plain fin heat exchanger with the smaller tube diameter and a fin spacing of 2.12 mm. Similar trends were observed for all the heat exchangers.

Figure 3.5 shows retained condensate divided by the total heat transfer area for the plain-fin-and-tube heat exchanger exposed to various air velocities. The heat exchangers were exposed to a range of face velocities between 0.8 m/s and 2.0 m/s. All three heat exchangers showed that in this range the effects of air-flow rate on condensate retention were minimal. The independence of condensate retention on air velocity agrees with McQuiston [3] who also found that under steady-state conditions over a Reynolds number range of 600 to 5000 a particular surface will hold a given amount of condensate regardless of the Reynolds number. The quantity of retained condensate was dependent on fin geometry and contact angles. As fin density increased the quantity of retained condensate also increased. The heat exchanger with a fin spacing of 2.12 mm retained approximately 90 g/m^2, and the quantity retained increased to about 120 g/m^2 for the heat exchanger with a fin spacing of 1.27 mm. These results were similar to the wavy-louvered experiments. The wavy-louvered heat exchangers that were tested also had fin spacings of 1.27, 1.59, and 2.12 mm. Figure 3.6 shows the three heat exchangers exposed to a range of air velocities between 0.8 m/s and 2.0 m/s. The retained condensate divided

by the total heat transfer area increased with increasing fin density. For the wavy-louvered heat exchanger with a fin spacing of 2.12 mm the quantity retained was approximately 100 g/m^2 and at a fin spacing of 1.27 mm the quantity retained increased to about 145 g/m^2.

Figure 3.7 compares the steady-state condensate retention per heat transfer area on plain-fin versus wavy-louvered heat exchangers for three different fin densities. The figure shows that at a given fin density the wavy-louvered heat exchangers hold more condensate than the plain-fin heat exchangers. The wavy-louvered heat exchangers retained anywhere from about 10 to 20% more water, depending on the fin spacing.

Wavy-louvered exchangers held more water than plain-fin exchangers because of condensate sweeping effects. In a wavy-louvered heat exchanger there is less sweeping and removing of condensate than for a plain-fin heat exchanger. Less removal of condensate occurs on a wavy-louvered heat exchanger than a plain-fin heat exchanger because of the differences in the maximum drop size and the number of drops that reach the maximum drop size. Because of the louvers, the maximum drop size found on a wavy-louvered heat exchanger will be smaller than that found on a plain-fin heat exchanger. This means that less droplets reach their maximum size and are removed from the heat exchanger. Since less droplets get removed, less condensate shedding occurs.

Air-Side Heat Transfer Results

In order to gain a better understanding of how condensate retention effects air-side heat transfer performance of plain-fin-and-tube and wavy-louvered heat exchangers, experiments were conducted and the sensible air-side heat transfer coefficients were

determined for both dry and wet conditions. The data reduction procedure used to determine the air-side heat transfer coefficient is outlined in ARI Standard 410 [18]. Details of the data reduction procedure are discussed in Appendix A.

Sensible j and friction factors

The sensible j factors and friction factors were calculated for all the heat exchangers under both wet and dry conditions. Equations 3.1 and 3.3 were used to calculate sensible j and friction factors, which allowed for comparison of heat transfer performance under the two different conditions.

$$j = StPr^{2/3} \tag{3.1}$$

$$St = \frac{Nu}{RePr} = \frac{h}{G_{air} Cp_{air}} \tag{3.2}$$

$$f = \frac{2\Delta P_{HX} \rho_{air}}{G^2}\left(\frac{A_{\min}}{A_{tot}}\right) - \left(1 + \left(\frac{A_{\min}}{A_{fr}}\right)^2\right)\left(\frac{\rho_{air,in}}{\rho_{air,out}} - 1\right)\left(\frac{A_{\min}}{A_{tot}}\right)\left(\frac{\rho_{air}}{\rho_{air,in}}\right) \tag{3.3}$$

where $\rho_{air} = \frac{\rho_{air,in} + \rho_{air,out}}{2}$ (3.4)

$$Re_{Dcoll} = \frac{GD_{coll}}{\mu_{air}} \tag{3.5}$$

Sensible j and f factors for the plain-fin-and-tube heat exchanger with the smaller tube diameter and a fin spacing of 2.12 mm are shown in Figure 3.8. The plot shows j and f for the heat exchanger under wet and dry conditions. An increase in f factor of approximately 40% is seen for the heat exchanger under wet conditions. The condensate that forms on a heat exchanger while operating under condensing conditions will restrict

flow and increase the pressure drop across the heat exchanger. A reduction in sensible j of about 70% was seen for the heat exchanger under condensing conditions. The reduction in j may be attributed to the condensation that accumulates on the heat exchanger surfaces. Other researchers have reported similar behavior. Jacobi and Goldschmidt [16] noticed lower wet j factors for heat exchangers operating at lower Reynolds numbers. Agreement was found by the work of Uv and Sonju [19] who showed that at Reynolds numbers based on tube collar diameter less than 2000 there was a degradation in sensible j factor under wet conditions.

Figure 3.9 shows sensible j and f factors for the plain-fin-and-tube heat exchangers with fin spacings of 1.27, 1.59, and 2.12 mm under both wet and dry conditions. For all three fin spacings the effect of condensation on air-side friction factor was significant. An increase in friction factor was seen across all three fin spacings for the plain-fin-and-tube heat exchangers under wet conditions. At fin spacings of 2.12 and 1.59 mm the difference between wet and dry f was approximately 45% whereas for the plain-fin heat exchanger with a fin spacing of 1.27 mm the difference increased to about 70%. The greater increase in friction factor seen for the heat exchanger with a fin spacing of 1.27 mm is due to condensate and fin geometry. Condensate bridges form between adjacent fins and as the fin spacing decreases the number of bridges increases. Condensate retention experiments showed that heat exchangers with tighter fin spacing will retain more water per heat transfer area. This was shown in Figure 3.5. The larger amount of retention found on heat exchangers with a tighter fin spacing will result in more restricted air-flow. The restricted air-flow will increase pressure drop across the heat exchanger, resulting in a higher friction factor. The effect of condensation on j was

also consistent for all three plain-fin heat exchangers -- decrease in j was seen under wet conditions. The difference in j seemed to be more significant as the fin spacing decreased. At a fin spacing of 2.12 mm the difference in j was approximately 50% and at a fin spacing of 1.27 mm the difference increased to approximately 120%. Condensate bridges that form more easily for heat exchangers with tighter fin spacings will decrease the amount of heat transfer area. The increased number of bridges may explain the more severe degradation in sensible j factor for the heat exchangers with tighter fin spacings.

The effects of condensation on j and f factors for wavy-louvered heat exchangers are shown in Figure 3.10. Sensible j and f factors under wet and dry conditions are shown for three different fin spacings of 1.27, 1.59, and 2.12 mm. An increase of approximately 30% in friction factor is seen for all three heat exchangers under wet conditions. Similar to the plain-fin heat exchangers, a decrease in j was seen under wet conditions. The decrease in j was more significant for the heat exchangers with wider fin spacing. For the wavy-louvered heat exchanger with a fin spacing of 1.27 mm, the difference in j under wet and dry conditions is approximately 50% whereas the difference increased to about 80% for the heat exchanger with a fin spacing of 2.12 mm. Increases in heat transfer performance can be attributed to fin geometry. For plain-fin heat exchangers the thermal boundary layer becomes thicker along the length of the fin. This will decrease the heat transfer coefficient. However, in a louvered fin heat exchanger the thermal boundary layer is restarted at each louver, thus maintaining a higher heat transfer coefficient. However, when a heat exchanger operates under wet conditions, condensate bridges fill up inter-louver gaps and the boundary layer is no longer restarted. A heat exchanger with a tighter fin spacing will form a greater number of bridges. The more severe degradation

in sensible j factor for the wavy-louvered heat exchangers with tighter fin spacings may be attributed to the increased number of condensate bridges.

A comparison was also made between the plain-fin-and-tube and wavy-louvered heat exchangers. Figure 3.11 shows j and f factors for two heat exchangers with the same fin spacing under dry and wet conditions. Under dry conditions, friction factor for the wavy-louvered heat exchanger was about 45% higher than for the plain-fin exchanger. The higher friction factor for the wavy-louvered heat exchanger is due to geometry differences. Air-flow is more interrupted in the wavy-louvered heat exchanger and a higher pressure drop results. Youn *et al.* [14] also found lower friction factors for plain-fin-and-tube heat exchangers under dry conditions. Compared to the plain-fin heat exchanger, the j factor was higher for the wavy-louvered heat exchanger under dry conditions. Over the range of Reynolds numbers tested, dry j was about 30% higher for the wavy-louvered heat exchanger. The higher sensible j for the wavy-louvered heat exchanger can be attributed to the higher heat transfer coefficient caused by the louvers that restart the thermal boundary layer. As shown in Figure 3.11b, the higher sensible j and friction factor found for the wavy-louvered heat exchanger under dry conditions disappeared once condensation formed on the heat exchangers.

Sensible j and f Factor Correlations

Sensible j and f factor correlations have been developed for plain-fin-and-tube and wavy-louvered heat exchangers under both wet and dry conditions. Table 3.1 shows the correlations developed for the heat exchangers. A Buckingham-Π analysis was used to

determine relevant dimensionless parameters and Equation 3.6 shows the proposed equation used for sensible j and f factor correlations for this research. Details of this analysis are described in Appendix B.

$$j, f = C(\mathrm{Re}_{Dcoll})^{a}\left(\frac{f_s}{D_{Coll}}\right)^{b} \tag{3.6}$$

where C, a, and b are constants.

A best fit multiple regression was found by minimizing the root mean square given in Equation 3.7. The root mean square was minimized with respect to the constants C, a, and b by using a variable metric search method.

$$root\ mean\ square = \sqrt{\frac{1}{n}\sum_{1}^{n}\left(X_{\exp,n} - X_{corr,n}\right)^2} \tag{3.7}$$

where n is the number of data points.

Figure 3.12 and Figure 3.13 show that the correlations that were developed for the plain-fin-and–tube heat exchangers estimated the j and f factors within 20% of the experimental data. Under dry conditions, 93% of the dry f were correlated within 20%, and 93% of dry j were within 20%. For wet conditions 86% of the wet f were correlated within 20%, and all wet j were within 20%. The correlations that were developed for the wavy-louvered heat exchangers also estimated the j and f factors within 20% of the experimental data. Figure 3.14 shows that under dry conditions, 94% of the dry f and dry j were within 20%. For wet conditions Figure 3.15 shows that the wet f and wet j data always fell within 20% of the correlation. Table 3.2 shows the root mean square values for the sensible j and f factor correlations developed for plain-fin and wavy-louvered heat exchangers under wet and dry conditions.

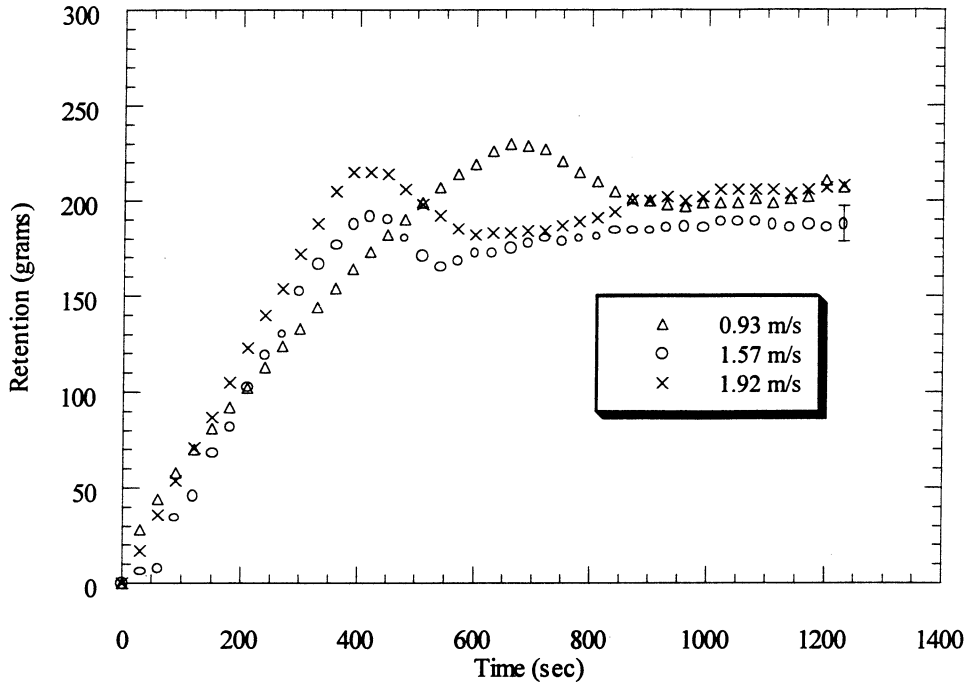

Figure 3.1 Real-time retention plot for a plain-fin-and-tube heat exchanger with a fin spacing of 2.12 mm exposed to various face velocities
Inlet Condition T_{in} ~ 34°C, $dewpoint_{in}$ ~23.9°C, $Tref_{in}$ ~ 2.8°C

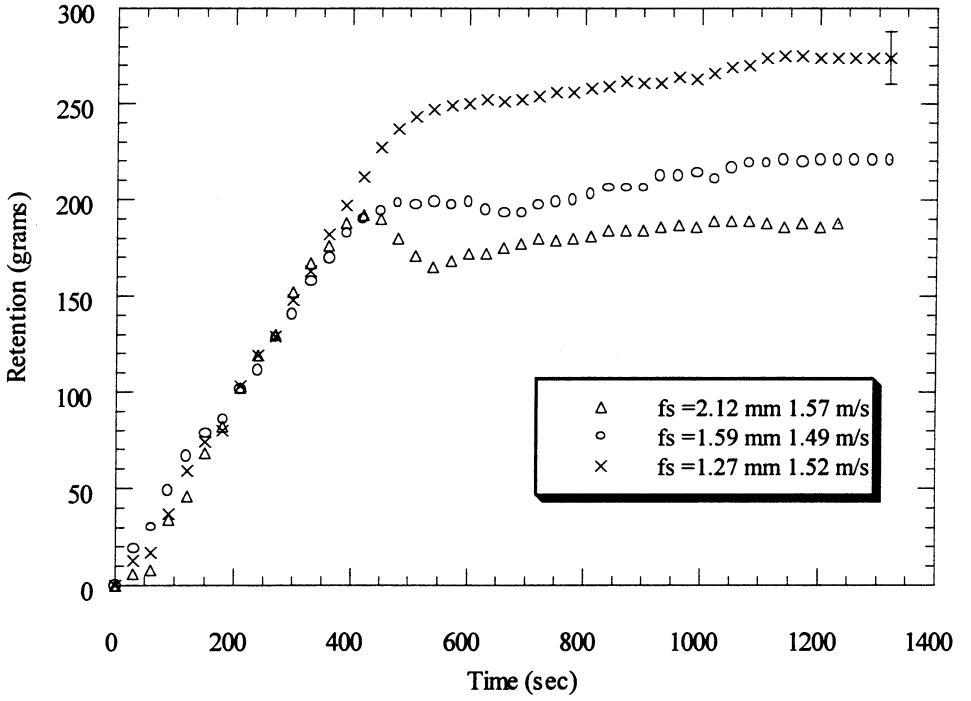

Figure 3.2 Real-time retention plot for plain-fin-and-tube heat exchangers with fin spacings of 1.27, 1.59, and 2.12 mm exposed to a fixed face velocity
Inlet Condition T_{in} ~ 34°C, $dewpoint_{in}$ ~23.9°C, $Tref_{in}$ ~ 2.8°C

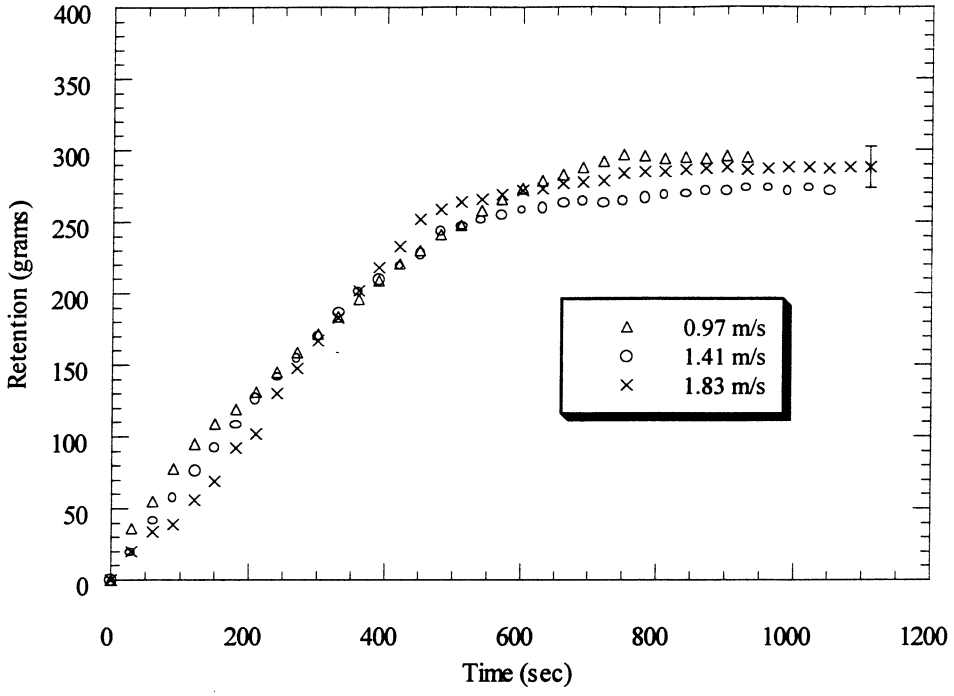

Figure 3.3 Real-time retention plot for a wavy-louvered heat exchanger with a fin spacing of 1.59 mm exposed to various face velocities
Inlet Condition T_{in} ~ 34°C, $dewpoint_{in}$ ~23.9°C, $Tref_{in}$ ~ 2.8°C

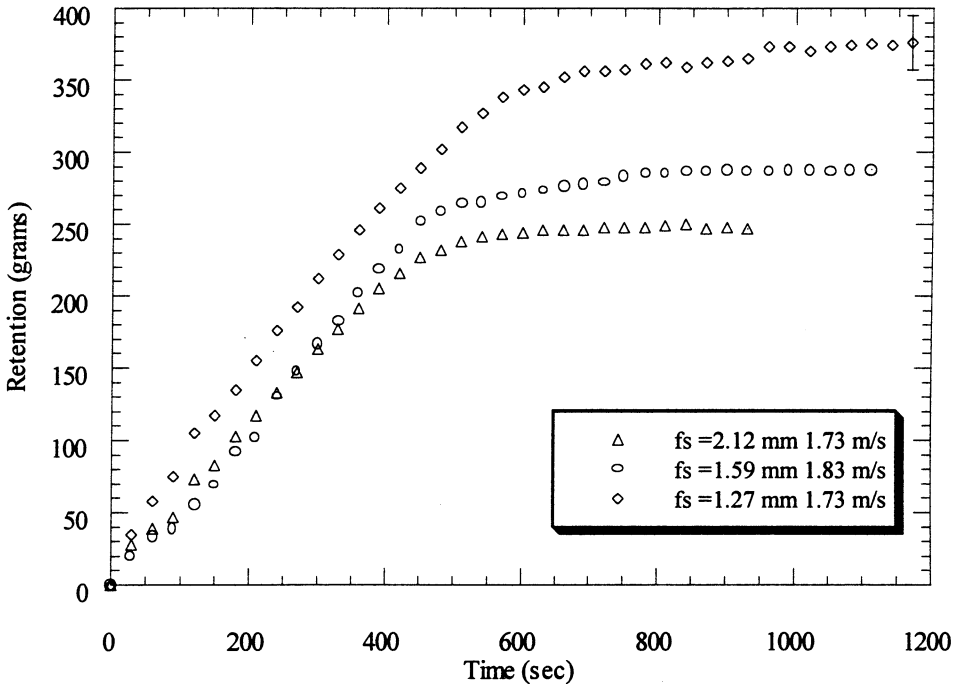

Figure 3.4 Real-time retention plot for wavy-louvered heat exchangers with fin spacings of 1.27, 1.59, and 2.12 mm exposed to a fixed face velocity
Inlet Condition T_{in} ~ 34°C, $dewpoint_{in}$ ~23.9°C, $Tref_{in}$ ~ 2.8°C

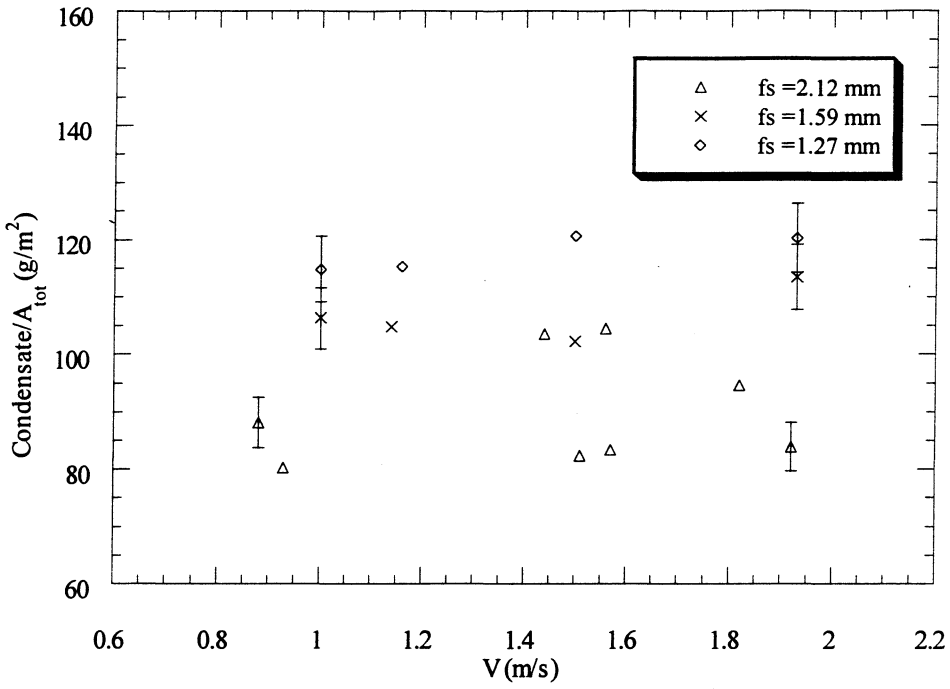

Figure 3.5 Condensate retention / A_{tot} for plain-fin-and-tube heat exchangers under steady-state conditions
Inlet Condition T_{in} ~ 34°C, $dewpoint_{in}$ ~23.9°C, $Tref_{in}$ ~ 2.8°C

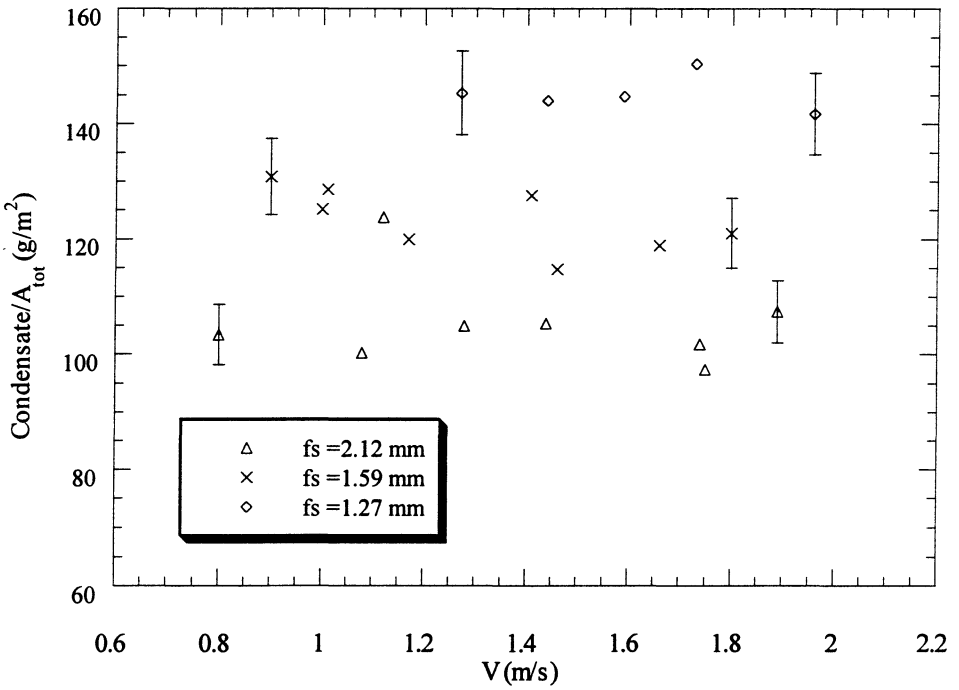

Figure 3.6 Condensate retention / A_{tot} for wavy-louvered heat exchangers under steady-state conditions
Inlet Condition T_{in} ~ 34°C, $dewpoint_{in}$ ~23.9°C, $Tref_{in}$ ~ 2.8°C

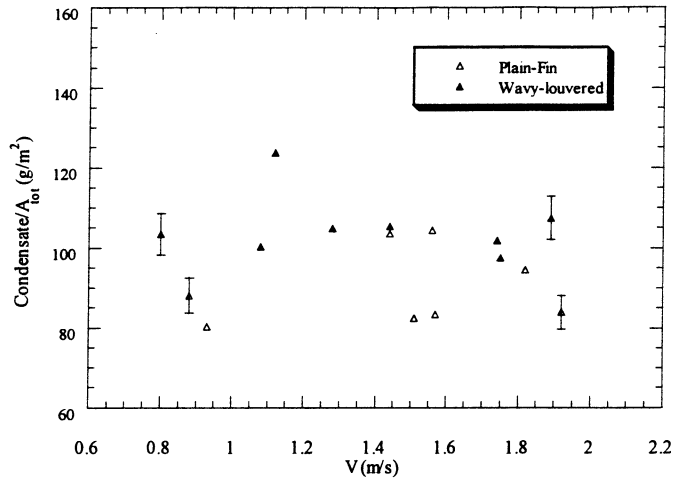

(a)

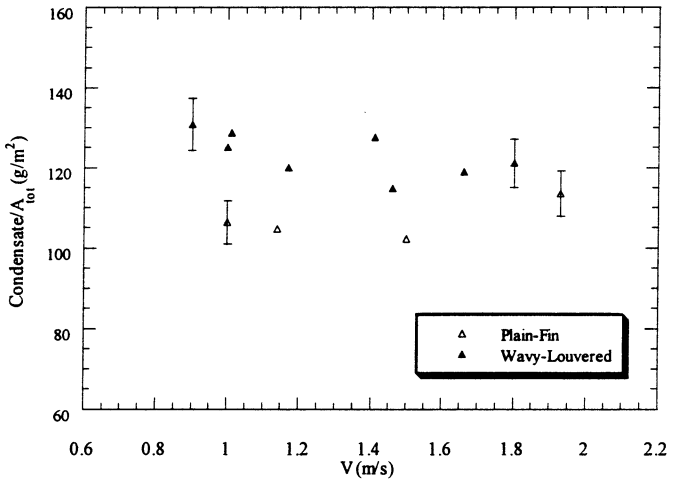

(b)

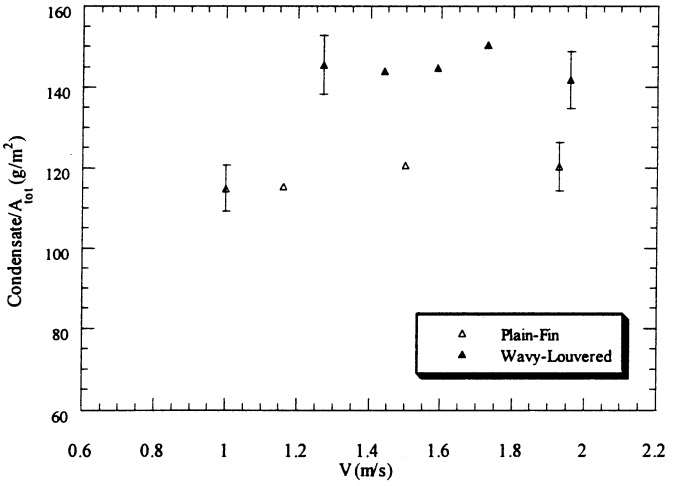

(c)

Figure 3.7 Steady-state condensate retention / A_{tot} for wavy-louvered versus plain-fin heat exchangers with varying fin spacings (a) 2.12 mm (b) 1.59 mm (c) 1.27 mm
Inlet Condition T_{in} ~ 34°C, $dewpoint_{in}$ ~23.9°C, $Tref_{in}$ ~ 2.8°C

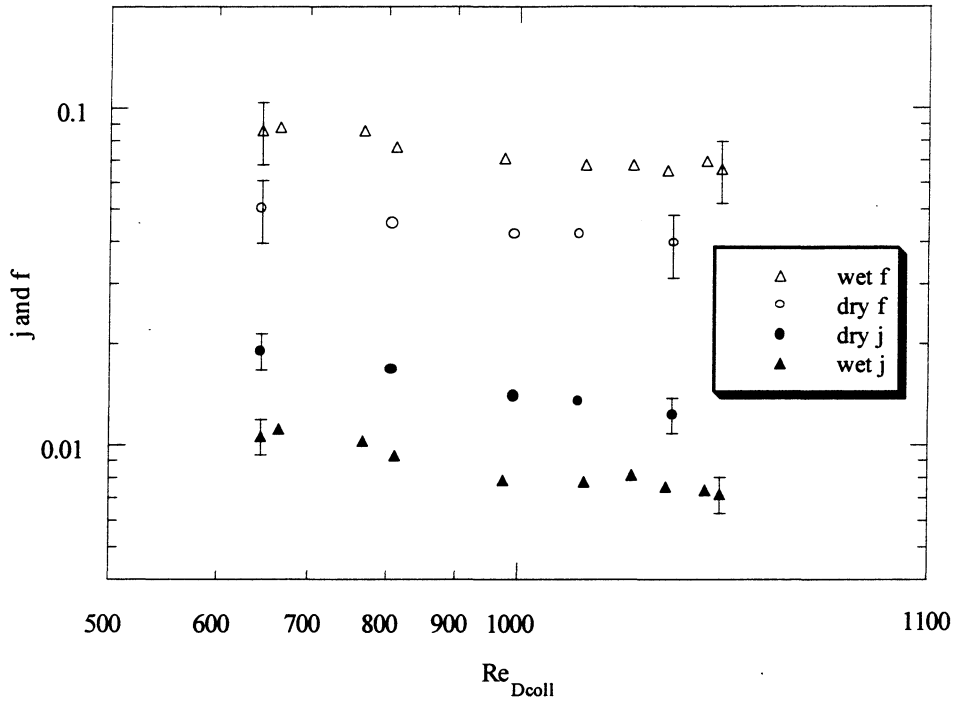

Figure 3.8 Sensible j and f for a plain-fin-and-tube heat exchanger with a fin spacing of 2.12 mm and a smaller tube diameter (D_{coll} = 7.11 mm)

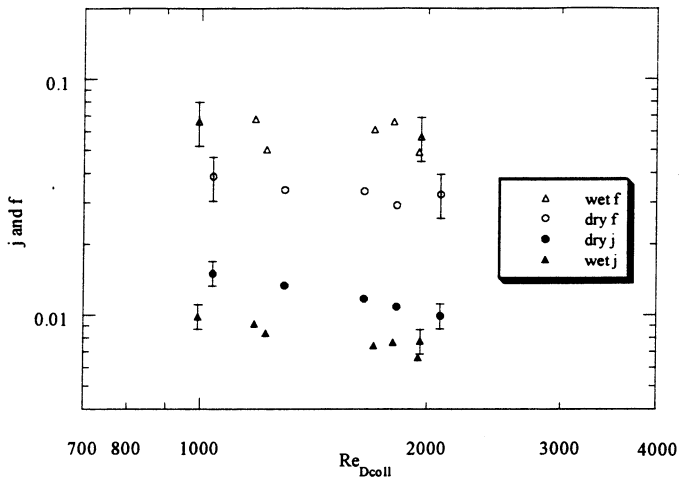

(a)

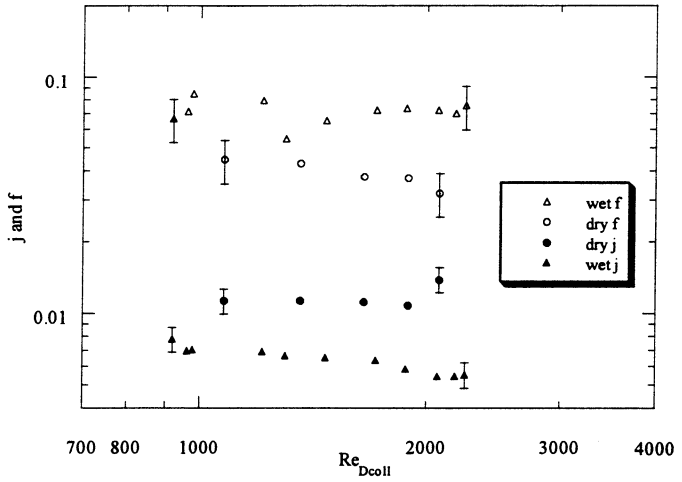

(b)

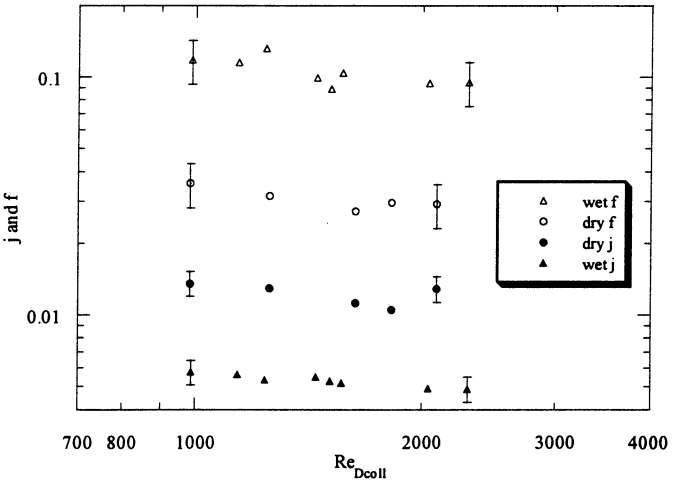

(c)

Figure 3.9 Sensible j and friction factor for plain-fin-and-tube heat exchangers with varying fin spacings (a) 2.12 mm (b) 1.59 mm (c) 1.27 mm

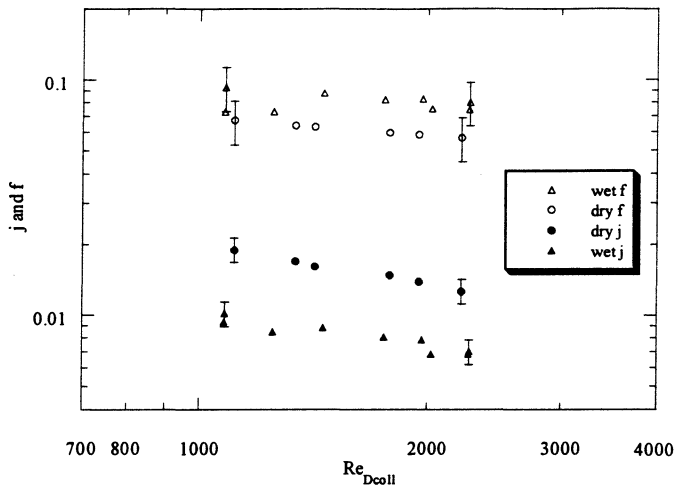

(a)

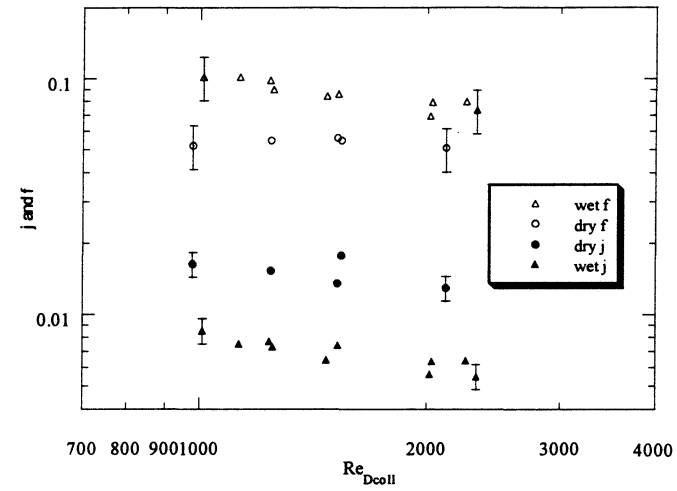

(b)

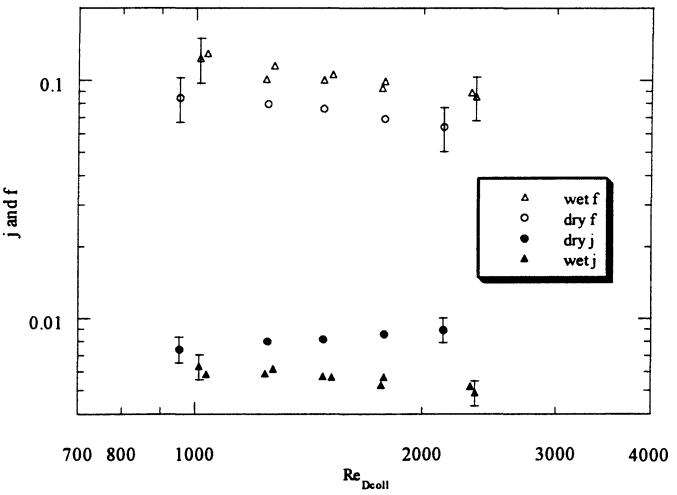

(c)

Figure 3.10 Sensible j and friction factor for wavy-louvered heat exchangers with varying fin spacings (a) 2.12 mm (b) 1.59 mm (c) 1.27 mm

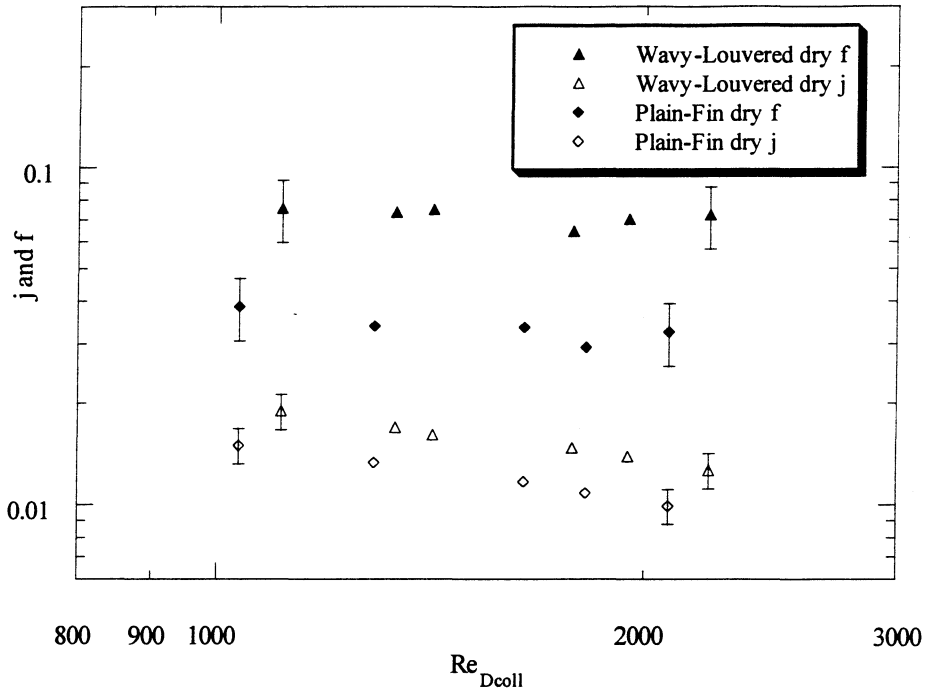

(a)

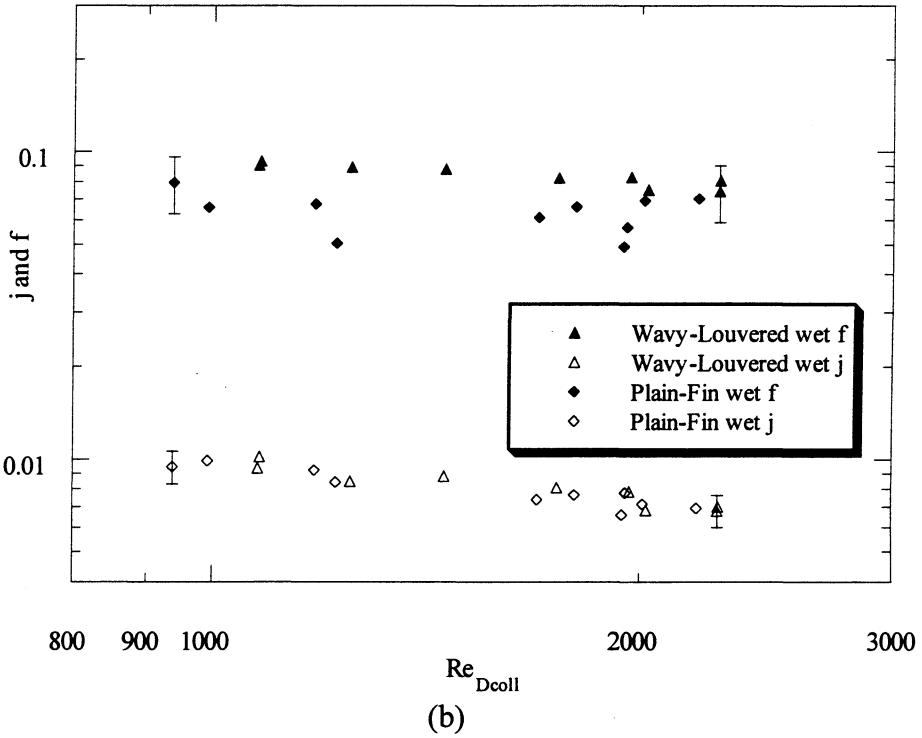

(b)

Figure 3.11 Sensible j and friction factor comparison for plain-fin versus wavy-louvered fin heat exchangers with the same fin spacing of 2.12 mm under (a) dry and (b) wet conditions

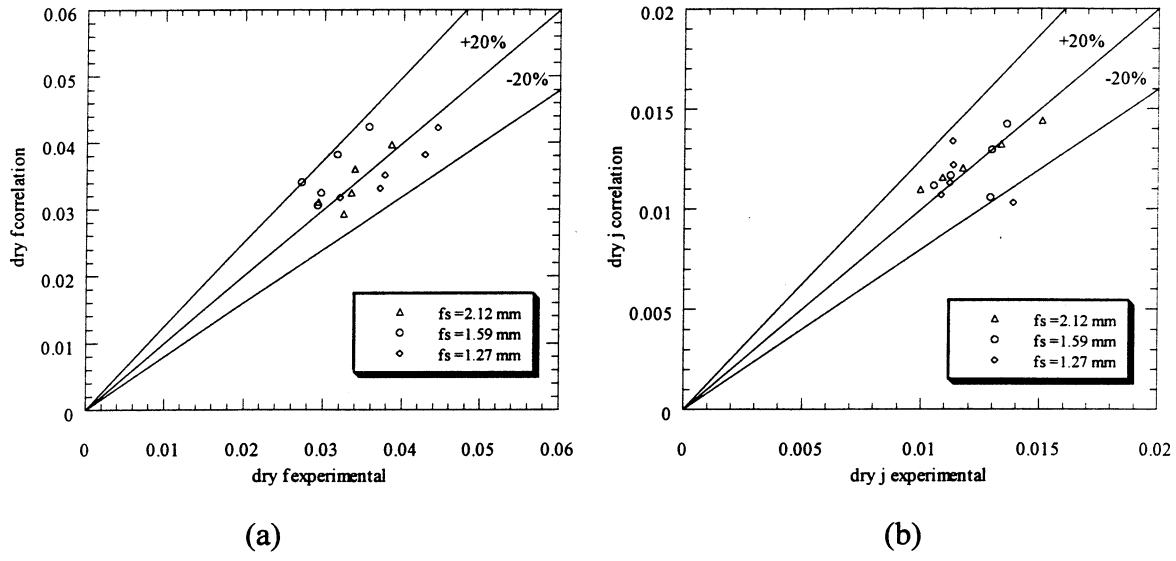

Figure 3.12 Comparison of (a) dry f and (b) dry j experimental data and correlation for plain-fin-and-tube heat exchangers with fin spacings from 1.27 to 2.12 mm

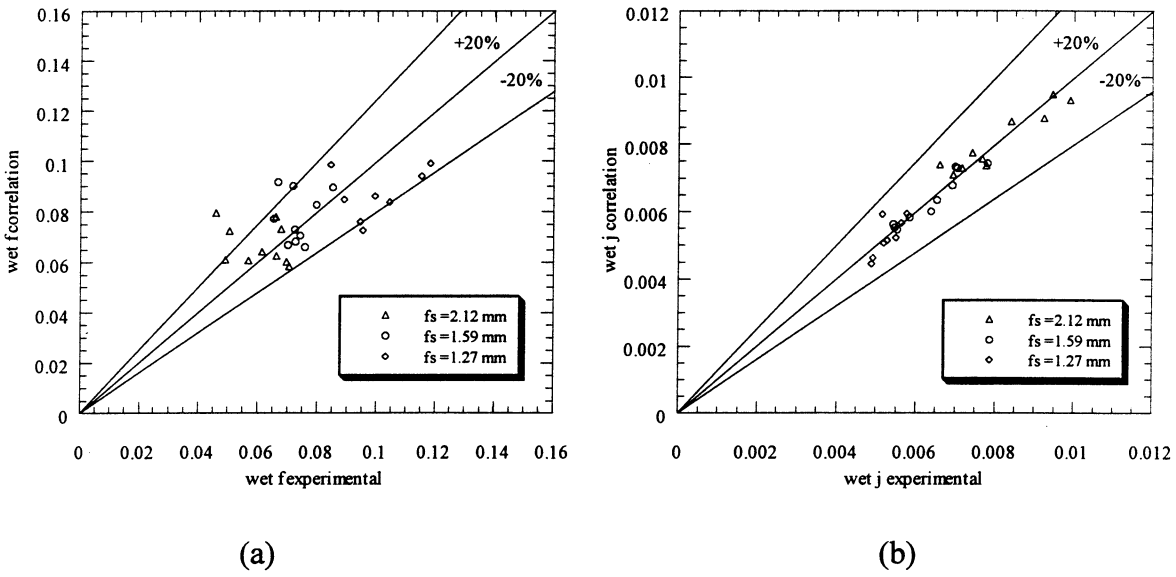

Figure 3.13 Comparison of (a) wet f and (b) wet j experimental data and correlation for plain-fin-and-tube heat exchangers with fin spacings from 1.27 to 2.12 mm

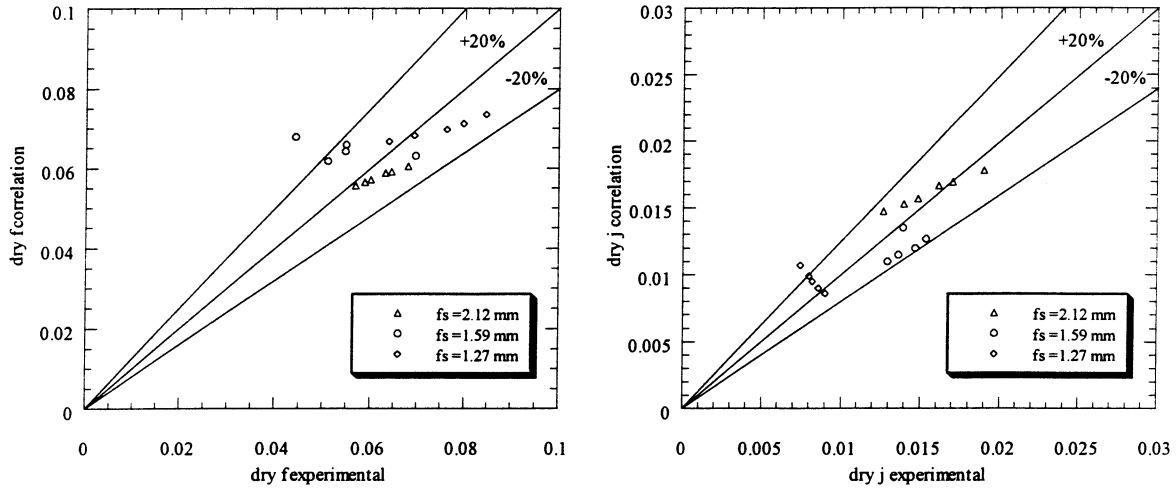

(a) (b)

Figure 3.14 Comparison of (a) dry f and (b) dry j experimental data and correlation for wavy-louvered heat exchangers with fin spacings from 1.27 to 2.12 mm

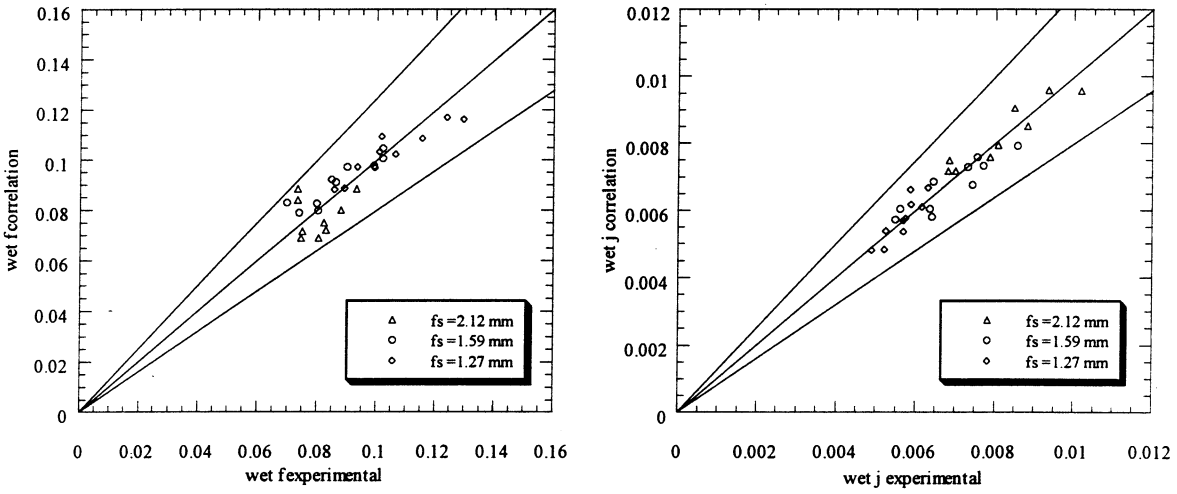

(a) (b)

Figure 3.15 Comparison of (a) wet f and (b) wet j experimental data and correlation for wavy-louvered heat exchangers with fin spacings from 1.27 to 2.12 mm

Table 3.1 Sensible j and f factor correlations for plain-fin-and-tube and wavy-louvered heat exchangers under wet and dry conditions.
Parameter range: $950 \leq Re_{Dcoll} \leq 2300$ and $1.27 \text{ mm} \leq f_s \leq 2.12 \text{ mm}$

Heat Exchanger	Condition	Correlation
Plain-Fin-and-Tube Uncoated	Dry	$f_{dry} = 0.6382(\text{Re}_{Dcoll})^{-0.4327}\left(\frac{f_s}{D_{Coll}}\right)^{-0.1442}$ $j_{dry} = 0.2651(\text{Re}_{Dcoll})^{-0.3945}\left(\frac{f_s}{D_{Coll}}\right)^{0.1098}$
	Wet	$f_{wet} = 0.4940(\text{Re}_{Dcoll})^{-0.3662}\left(\frac{f_s}{D_{Coll}}\right)^{-0.4326}$ $j_{wet} = 0.3627(\text{Re}_{Dcoll})^{-0.3445}\left(\frac{f_s}{D_{Coll}}\right)^{0.8169}$
Wavy-Louvered Uncoated	Dry	$f_{dry} = 0.08515(\text{Re}_{Dcoll})^{-0.1209}\left(\frac{f_s}{D_{Coll}}\right)^{-0.3215}$ $j_{dry} = 0.5737(\text{Re}_{Dcoll})^{-.2691}\left(\frac{f_s}{D_{Coll}}\right)^{1.008}$
	Wet	$f_{wet} = 0.437(\text{Re}_{Dcoll})^{-0.3357}\left(\frac{f_s}{D_{Coll}}\right)^{-0.4745}$ $j_{wet} = 0.4393(\text{Re}_{Dcoll})^{-0.3894}\left(\frac{f_s}{D_{Coll}}\right)^{0.7028}$

Table 3.2 Root mean square values for sensible j and f factor correlations developed for plain-fin and wavy-louvered heat exchangers under wet and dry conditions

	Plain-Fin		Wavy-Louvered	
	Dry	Wet	Dry	Wet
f factor	10.5	22.3	17.2	8.6
Sensible j	9.5	5.3	16.4	5.8

Chapter 4 – Modeling Condensate Retention

By calculating the total volume of retained condensate on a plain-fin heat exchanger and multiplying the volume by the density of water the mass of retained condensate on a heat exchanger surface may be determined. For this research the volume of the retained condensate is estimated by droplets adhering to the fin surfaces and bridges between adjacent fins at fin-tube junctions. A force balance is used to determine the maximum size for each condensate geometry. Using digital image analysis a droplet distribution smaller than the maximum size may be found along with the percentage of the total heat transfer area that is covered with condensate. A good estimate for the mass of retained condensate may then be calculated after the maximum size, the droplet distribution, and the area covered are determined.

Retained Condensate Size Distribution

The approach used to find condensate size distributions was similar to Graham [20] who determined droplet size distributions for dropwise condensation on a vertical mirror-smooth copper surface at atmospheric pressure. Equations 4.1 and 4.2 show the form used in Graham's distributions.

$$\Delta N = B_1 D^{-1.73} \qquad \text{for } 10\mu\text{m} < D < 0.2D_{max} \qquad (4.1)$$

$$\Delta N = B_2 D^{-2.8} \qquad \text{for } 0.2\,D_{max} < D < D_{max} \qquad (4.2)$$

where

ΔN is the number of drops of diameter D±0.2D per cm^2

Graham found a change in the droplet distribution at a droplet diameter of 500 micrometers attributed it to droplet departure mechanisms for drops larger than 500 micrometers and coalescence of droplets for drops smaller than 500 micrometers. The maximum drop diameter observed by Graham was 2500 micrometers. The largest drop diameter found in this research was much larger than that found by Graham but a change in distribution was found to occur at approximately the same D/D_{max}.

For this research, the droplet distribution is difficult to determine from the heat exchangers because of the tight fin spacing. Therefore instead of studying the droplet distribution on the heat exchanger, a stock fin sample was exposed to condensing conditions inside a glove box and photographs were recorded. Various locations on the fin were recorded so that the variation in drop distributions for different parts of a fin could be determined. Furthermore, the amount of surface area covered by drops varies along a heat exchanger fin and by studying various locations and determining how much of the surface is covered by drops for each location, a more accurate model could be developed. The selected areas that were studied for the stock fin sample that was exposed to condensing conditions are shown in Table 4.1. The photographs were recorded at distances of approximately 5.1, 10.2, and 15.3 cm from the top of the fin sample and are named as the top, middle and bottom sections respectively. The droplets were colored black to increase the accuracy of the image analysis done by Scion Image. Scion Image calculated the area of each droplet and an equivalent diameter was determined using Equation 4.3 for each droplet.

$$D_{equiv} = \sqrt{\frac{4A_{scion}}{\pi}} \tag{4.3}$$

Droplet distributions and percentage of heat transfer area covered by condensate droplets was determined for each section and results are shown in Table 4.2. A variable bin size with drop diameter D±0.1D was used to determine the distributions. The results obtained from each section were then used to characterize the droplet distribution and area coverage for the top, middle, and bottom sections of a heat exchanger. The percentage of heat transfer area covered by droplets was similar for the top and middle sections; however a big decrease in area covered was seen for the bottom section. This can be attributed to sweeping effects where the bottom section will be affected by all the droplets that sweep from the above two sections.

Retained Condensate Geometries

The total quantity of retained condensate is estimated by considering two condensate geometries. Condensate was observed to accumulate as droplets adhering to the fin surfaces and as bridges between adjacent fins at fin-tube junctions. Korte and Jacobi [9] developed equations to calculate the volume of droplets and bridges. Force balances were used to determine the maximum sizes of the condensate droplets and bridges.

Figure 4.1 shows a droplet adhering to surface with a circular contact line and at an inclination angle of α. The heat exchangers used for this research had vertical fin surfaces or an inclination angle of $\alpha = \pi/2$. The equation used to calculate the volume of a droplet is given by Equation 4.4 as a function of the mean contact angle and diameter of the droplet.

$$V_{drop} = \frac{\pi D_{drop}^3}{24}\left(\frac{2-3\cos\theta_M+\cos^3\theta_M}{\sin^3\theta_M}\right) \tag{4.4}$$

where

$$\theta_M = \frac{\theta_A+\theta_R}{2}$$

Applying a force balance on the condensate droplet shown in Figure 4.1 will give an estimate for the maximum droplet diameter. The balance between gravitational, surface tension, and air-flow forces as shown in Equation 4.5 may be used to determine the maximum droplet size.

$$F_{gy}+F_{sy}+F_{dy}=0 \tag{4.5}$$

where

$$F_{gy} = -\rho_l g \forall \sin\alpha$$

$$F_{sy} = \frac{\gamma D}{2}\left[\frac{\sin\theta_R-\sin(\theta_A-\pi)}{\left(\frac{\theta_R-\theta_A}{\pi}\right)+1}+\frac{\sin\theta_R-\sin(\theta_A+\pi)}{\left(\frac{\theta_R-\theta_R}{\pi}\right)-1}\right]$$

Condensate retention experiments showed that the quantity of retained condensate was independent of air-side Reynolds number so the proposed model will assume the air-flow forces to be negligible in the y-direction. The maximum droplet diameter for the plain-fin-and-tube heat exchangers used in this research can then be determined from a balance between the gravitational and surface tension forces. The maximum droplet diameter that was observered from the glove box experiments was also measured using Scion Image. Table 4.3 shows that the maximum droplet diameter obtained from the force balance analysis is in good agreement with the droplet diameters measured from the glove box

experiments. Although the droplet distribution and percentage of area covered varied between the top, middle, and bottom sections, the measured diameters from the glove box experiments show that the maximum droplet diameter does not change between different sections.

Figure 4.2 shows a condensate bridge between adjacent fins at a fin-tube junction. Similar to the condensate droplets, Korte and Jacobi [9] determined the maximum size of a fin-tube bridge by a force balance between surface tension and gravitational forces. The surface tension forces in the y direction are given in Equation 4.6 and 4.7.

$$F_{S1} = 2\gamma l \cos(\pi - \theta_A) \tag{4.6}$$

$$F_{S2} = 2\gamma f_s \cos(\theta_R) \tag{4.7}$$

The opposing gravitational force is given by Equation 4.8.

$$F_g = -\rho_l g \forall \tag{4.8}$$

Equation 4.9 is used to calculate the volume of a fin-tube bridge.

$$\forall_{bridge} = L_{\max}(l \cdot f_s) - A_1 f_s + A_2 l \tag{4.9}$$

where

$$A_1 = (\pi R_1^2)\left(\frac{\pi/2 - \theta_R}{\pi}\right) - \frac{l}{2}\left[R_1^2 - \left(\frac{l}{2}\right)^2\right]^{1/2}$$

$$A_2 = (\pi R_2^2)\left(\frac{\theta_A - \pi/2}{\pi}\right) + \frac{f_s}{2}\left[R_2^2 - \left(\frac{f_s}{2}\right)^2\right]^{1/2}$$

and

$$R_1 = \frac{D_{coll}}{2}$$

$$R_2 = \frac{f_s}{2\sin\left(\theta_A - \pi/2\right)}$$

By using Equation 4.6 through Equation 4.9, neglecting air-flow forces, and applying a force balance in the y direction the maximum length of the fin-tube bridge can be determined.

$$L_{\max} = \frac{2\gamma f_s \cos\theta_R + 2\gamma l\cos(\pi - \theta_A) + \rho_l g A_1 - \rho_l g l A_2}{\rho_l g l f_s} \tag{4.10}$$

where γ is the surface tension of water. Equation 4.11 shows a relationship which was developed by Jasper [21] to determine the surface tension as a function of temperature given in degrees Celsius.

$$\gamma(mN/m) = 75.83 - 0.1477T \tag{4.11}$$

which is valid over a temperature range of $10°C \leq T \leq 100°C$.

Proposed Retention Model

The total mass of retained condensate may be estimated by summing the mass of condensate contributed by droplets with the contribution by fin-tube bridges as shown in Equation 4.12. Details of the condensate retention model are discussed in Appendix D.

$$M = A_T \rho \int_{20\mu m}^{D_{\max}} \overline{N}_D \forall_D dD + \rho \forall_{bridge} N_{tr} N_f \tag{4.12}$$

Several assumptions were made to estimate the mass of retained condensate. The plain-fin-and-tube heat exchanger was assumed to be fully wet. The droplet distributions on the fin surfaces are not effected by droplets on adjacent fin surfaces. Bridges only occur at

the fin-tube junction and not between adjacent fins. Finally, it was assumed that all of the fin-tube regions were filled with condensate bridges of length L_{max} determined by Equation 4.7.

Retention Modeling Results

After determining the droplet distributions, percentage of heat transfer areas covered by condensate droplets, and contact angles the total volume and mass of retained condensate can be estimated. Table 4.4 shows a comparison between measured mass of retained condensate from the experiments and the predicted mass of retained condensate given by the model. The comparison is made for three of the plain-fin-and-tube heat exchangers with fin spacings of 1.27, 1.59, and 2.12 mm. The measured mass of retained condensate is from experiments with the heat exchangers exposed to an air velocity range of approximately 0.8 m/s to 2.0 m/s. The model predicted the mass of retained condensate based on maximum droplet diameters determined from the force balance analysis and from droplets measured from the glove box experiments. Furthermore, contact angles from an unexposed fin surface and contact angles from a fin surface exposed to prolonged condensing conditions were used to compare the quantity of retained condensate on fins with different characteristics. The results show that the mass of retained condensate estimated by the model with contact angles typical of an exposed fin surface is within the range of the measured mass for the heat exchanger with a fin spacing of 2.12 mm. However, the mass of condensate estimated by the model is higher than the measured mass for the exchangers with a fin spacing of 1.59 and 1.27 mm. The discrepancy is more pronounced with increasing fin density and can be attributed to the assumption that

droplets on the fin surfaces are not effected by droplets on adjacent fin surfaces. For the heat exchangers with higher fin density there is an increased likelihood of droplets on a fin surface interacting with droplets on an adjacent surface. Bridges may form between droplets on adjacent fins and increased sweeping may occur reducing the quantity of retained condensate. Furthermore, the maximum diameter of droplets predicted by the model was greater than the measured values. Table 4.5 shows the predicted maximum quantity of retained condensate as fin-tube bridges. The values shown should overestimate the quantity of retained condensate because not all of the regions downstream of the tubes will be filled with bridges. Although the model for the plain-fin-and-tube heat exchangers overestimated the quantity of retained condensate, the model was relatively good considering the complex physics involved.

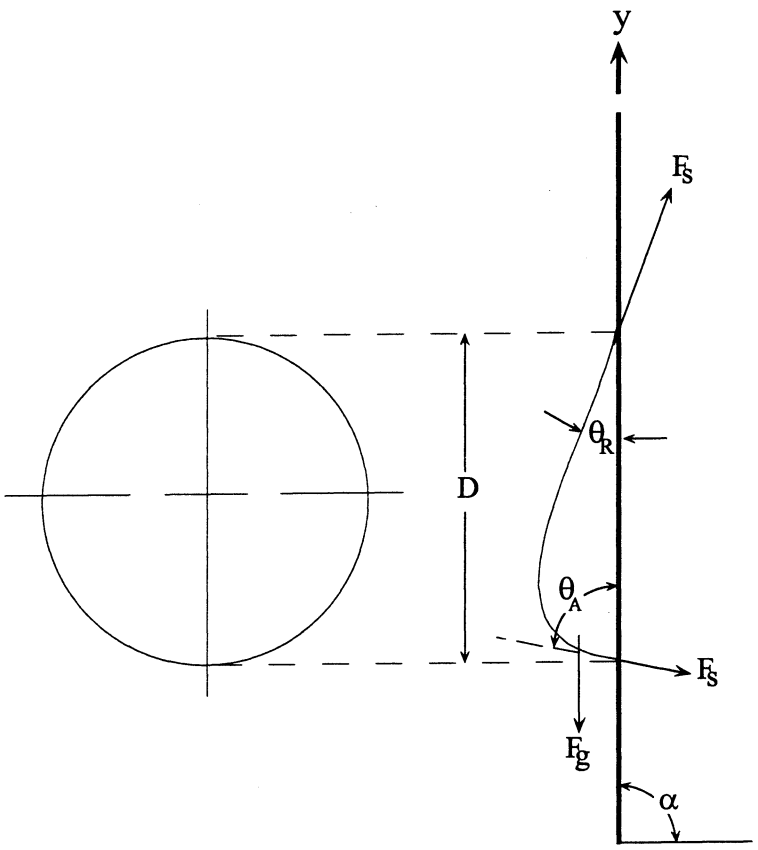

Figure 4.1 Droplet adhering to a surface with a circular contact line at an inclination angle of $\alpha = \pi/2$ (adopted from [9])

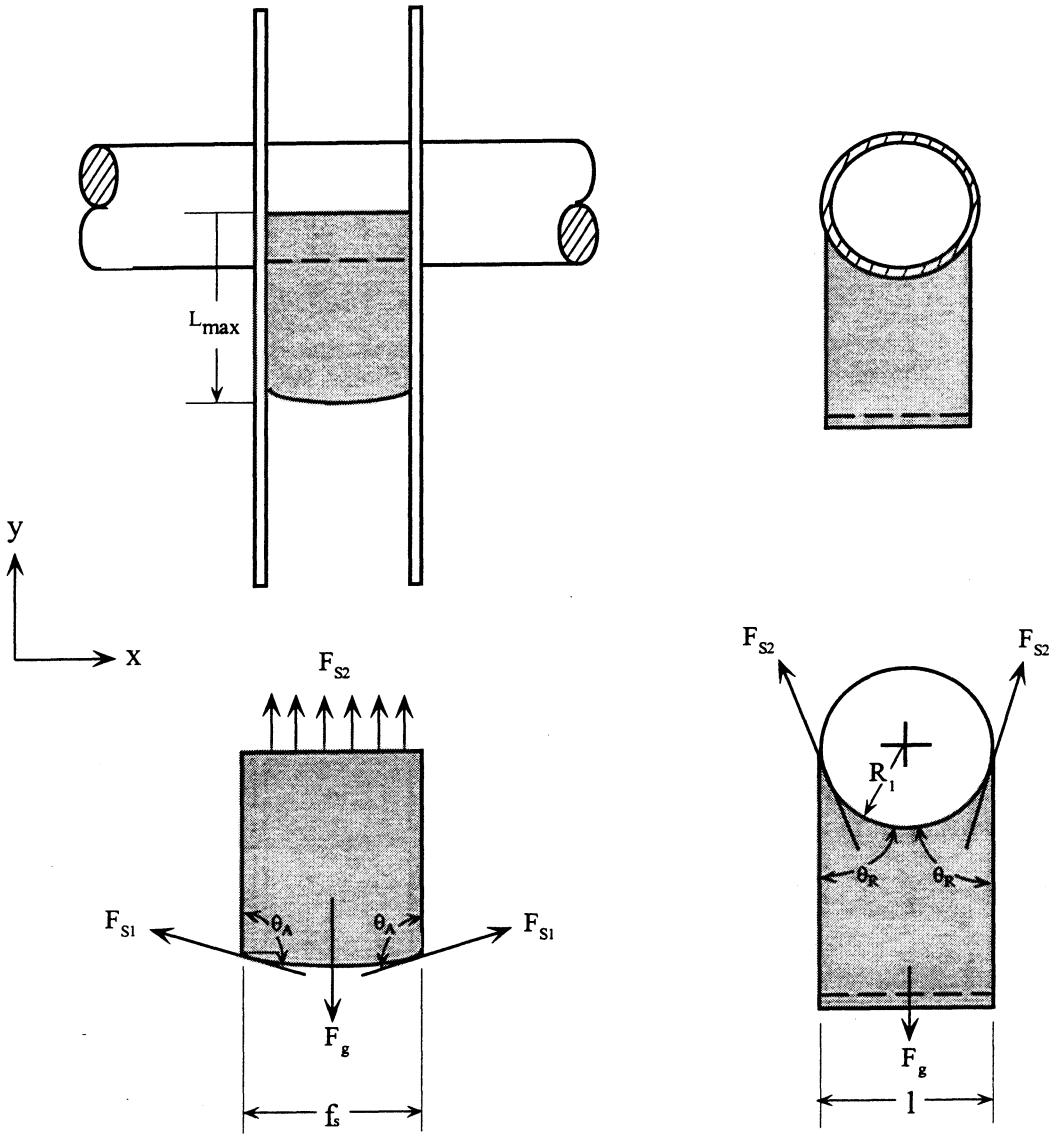

Figure 4.2 Forces acting on bridges retained between fins at fin-tube junction [9]

Table 4.1 Photographs of a stock fin sample that was exposed to condensing conditions at various locations.

	Original photograph	Condensate droplets colored black
Top	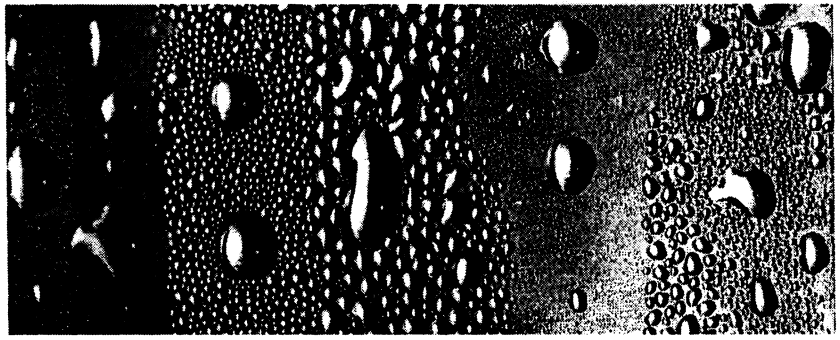	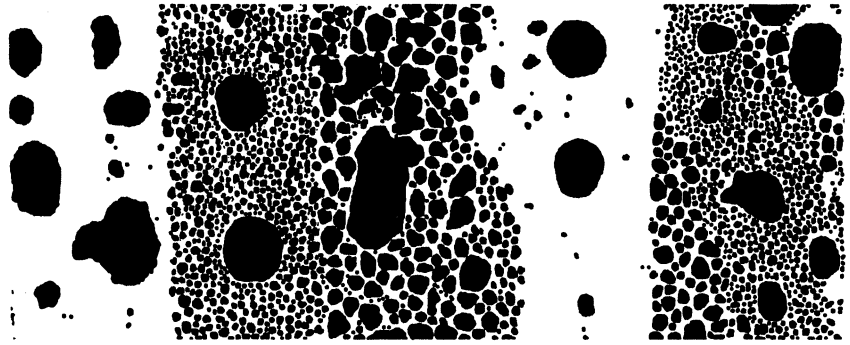
Middle	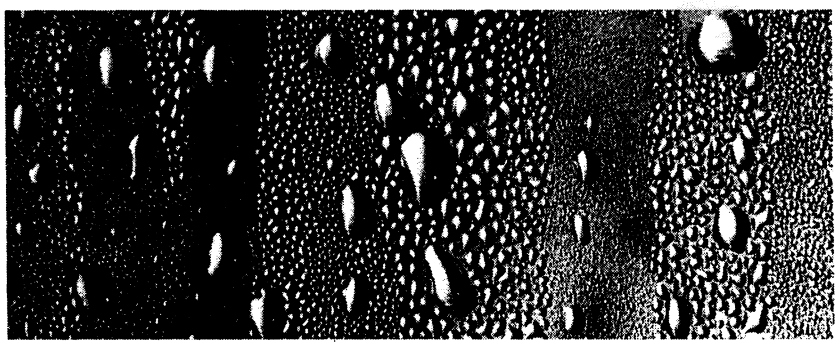	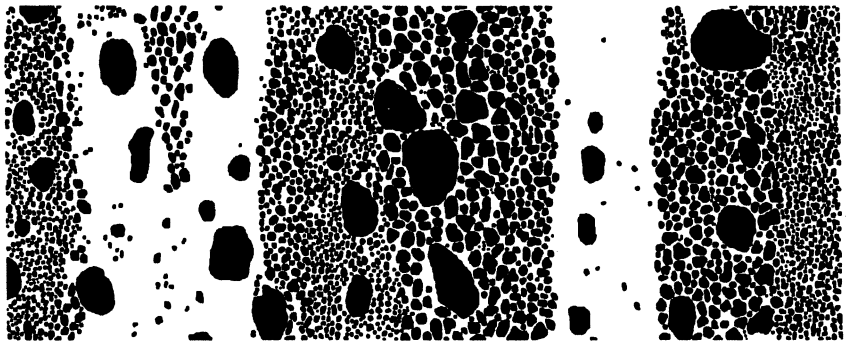
Bottom	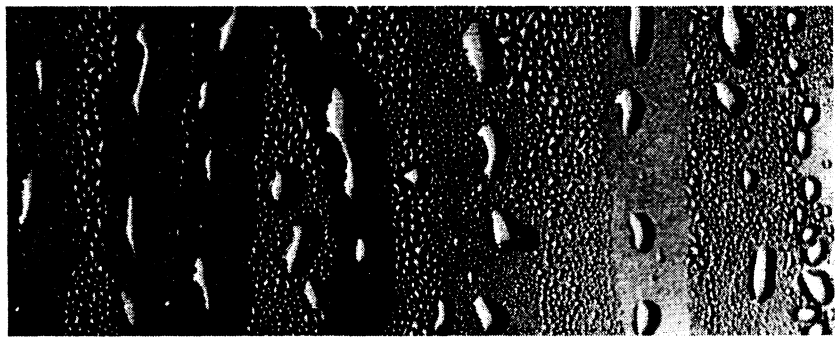	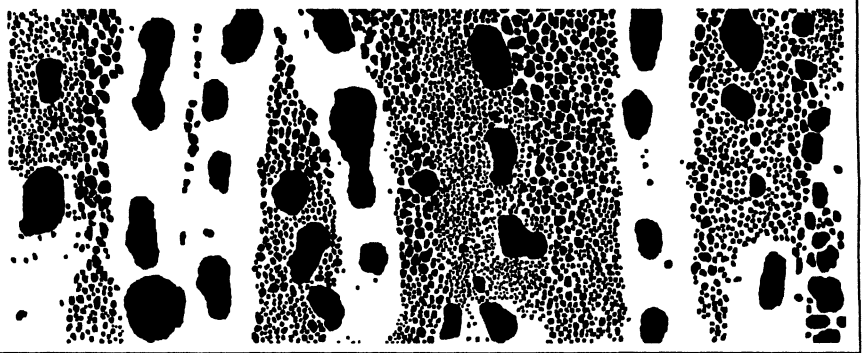

Table 4.2 Droplet size distributions and percentage of heat transfer area covered by condensate droplets for stock fin sample at various locations.

	$20\mu m < D < 0.2D_{max}$		$0.2\ D_{max} < D < D_{max}$	
	% Area covered	$\Delta N/\Delta D$	% Area covered	$\Delta N/\Delta D$
Top	19.1	$2.05\text{x}10^{9}\ D^{-2.74}$	22.7	$3.44\text{x}10^{8}\ D^{-2.37}$
Middle	23.2	$8.41\text{x}10^{8}\ D^{-2.60}$	18.6	$5.24\text{x}10^{8}\ D^{-2.47}$
Bottom	5.4	$1.93\text{x}10^{6}\ D^{-2.61}$	12.5	$7.08\text{x}10^{9}\ D^{-2.96}$

Table 4.3 Comparison of maximum droplet diameters determined from model and droplet diameters measured from glove box experiments.

	$D_{max,measured}$ (mm)	$D_{max,model}$ (mm)	
		$\theta_A = 89.6°\ \theta_R = 42.4°$	$\theta_A = 85.5°\ \theta_R = 37.3°$
Top	4.2	4.8	4.9
Middle	4.4	4.8	4.9
Bottom	4.3	4.8	4.9

Table 4.4 Comparison between measured mass of retained condensate and predicted mass of condensate on heat exchanger surface.

Plain-fin heat exchanger	Measured mass of retained condensate (g)	Predicted mass of retained condensate (g)			
		$\theta_A = 89.6°\ \theta_R = 42.4°$		$\theta_A = 85.5°\ \theta_R = 37.3°$	
		$D_{max,\ measured}$	$D_{max,\ model}$	$D_{max,\ measured}$	$D_{max,\ model}$
$f_s = 2.12$ mm	186 – 242	250	273	212	237
$f_s = 1.59$ mm	237 – 264	315	347	264	298
$f_s = 1.27$ mm	267 – 281	380	421	315	357

Table 4.5 Predicted mass of condensate retention as fin-tube bridges.

Plain-fin heat exchanger	Predicted mass of retained condensate (g)	
	$\theta_A = 89.6°$ $\theta_R = 42.4°$	$\theta_A = 85.5°$ $\theta_R = 37.3°$
$f_s = 2.12$ mm	50	33
$f_s = 1.59$ mm	48	25
$f_s = 1.27$ mm	47	16

Chapter 5 – Conclusions and Recommendations

In this chapter the conclusions drawn from the condensate retention and heat transfer experiments conducted on plain-fin-and-tube and wavy-louvered heat exchangers are presented. A model was developed for plain-fin heat exchangers and conclusions are presented here as well. Furthermore, recommendations for future experimental work and condensate retention modeling are discussed.

Real-time and Steady-state Condensate Retention

- Real-time retention for the plain-fin-and-tube heat exchangers showed a pronounced maximum behavior. The mass of retained condensate increased until reaching a maximum. Shortly after reaching the maximum, the quantity of retained condensate dropped but would eventually reach a steady value, reflecting an equilibrium between condensate deposition and shedding. However, as the fin density for the plain-fin-and-tube heat exchangers increased the pronounced maximum behavior disappeared. Instead of having a pronounced maximum behavior, the mass of retained condensate steadily increased and approached a maximum value. This steady increase in condensate retention behavior was similar to that seen for the wavy-louvered heat exchangers with fin spacings of 1.27, 1.59, and 2.12 mm.
- Steady-state condensate retention experiments showed that the quantity of retained condensate was independent of air flow velocities in the rage of this study. The quantity of retained condensate was dependent on fin geometry and contact angles. For both plain-fin and wavy-louvered heat exchangers the retained condensate

divided by the total heat transfer area increased with increasing fin density. At the same fin spacing the quantity of retained condensate for a plain-fin heat exchanger was about 10 to 20% less than for the wavy-louvered heat exchanger, depending on the fin spacing.

Air-Side Heat Exchanger Performance

- An increase in f factor was seen for the plain-fin and wavy-louvered heat exchangers when tested under wet conditions. The condensate that forms on a heat exchanger under condensing conditions will restrict flow and increase the pressure drop across the heat exchanger which increases the f factor. For the plain-fin-and-tube heat exchanger with a fin spacing of 2.12 mm the increase in f factor under wet conditions was approximately 45%, whereas the increase in f factor increased to about 70% when the fin spacing decreased to 1.27mm. For the wavy-louvered heat exchangers the increase in f factor under wet conditions was about 30% for all the fin spacings tested.
- A degradation in sensible j was observed for the plain-fin-and-tube heat exchangers under condensing conditions. The difference in j seemed to be more significant as the fin spacing decreased. At a fin spacing of 2.12 mm the difference in j was approximately 50% and at a fin spacing of 1.27 mm the difference increased to about 120%. The reduction in j may be attributed to the condensation that accumulates on the heat exchanger surfaces. Condensate bridges that form more easily for heat exchangers with tighter fin spacings will decrease the amount of heat transfer area.

The increased number of bridges may explain the more severe degradation in sensible j factor for the heat exchangers with tighter fin spacings.

- For the wavy-louvered heat exchangers a decrease in j was also seen under wet conditions. The decrease in j was more significant for the heat exchangers with wider fin spacing. For the wavy-louvered heat exchanger with a fin spacing of 1.27 mm, the difference in j under wet and dry conditions is approximately 50% whereas the difference increased to about 80% when the fin spacing increased to 2.12 mm.
- A comparison was also made between the plain-fin-and-tube and wavy-louvered heat exchangers with the same fin spacing. Under dry conditions, friction factor and j factor for the wavy-louvered heat exchanger was higher than for the plain-fin exchanger. The higher sensible j for the wavy-louvered heat exchanger can be attributed to the higher heat transfer coefficient caused by the louvers that restart the thermal boundary layer. The higher sensible j factor found for the wavy-louvered heat exchanger under dry conditions disappeared once condensation formed on the exchanger because when a heat exchanger operates under wet conditions, condensate bridges fill up inter-louver gaps and the boundary layer is no longer restarted.

Condensate Retention Modeling

- A force balance between gravitation and surface tension forces was used to determine the maximum droplet diameter for the plain-fin-and-tube heat exchangers used in this research. The maximum droplet diameter that was determined from the force balance

analysis was found to be in good agreement with the maximum droplet diameter that was observered from the glove box experiments.

- A stock fin sample was exposed to condensing conditions inside a glove box and photographs were recorded to determine droplet distribution and the percentage of heat transfer area covered by drops. Various locations on the fin were recorded so that the drop distributions and area covered for different parts of a fin could be determined. The percentage of heat transfer area covered by droplets was similar for the top and middle sections, however a big decrease in area covered was seen for the bottom section. This can be attributed to sweeping effects where the bottom section will be affected by all the droplets that sweep from the above two sections.
- Modeling results show that the mass of retained condensate estimated by the model with contact angles typical of an exposed fin surface is within the range of the measured mass for the heat exchanger with a fin spacing of 2.12 mm. However, the mass of condensate estimated by the model is higher than the measured mass for the heat exchangers with fin spacings of 1.57 and 1.27 mm. The discrepancy is more pronounced with increasing fin density and can be attributed to the assumption that droplets on the fin surfaces are not effected by droplets on adjacent fin surfaces. Similar to Korte and Jacobi [9], the modeling results from this research were relatively successful in predicting the quantity of retained condensate for heat exchangers with wider fin spacings where the droplet distributions were independent of droplets on adjacent fins.

Recommendations for Future Studies

- In order to improve the condensate retention model and to better understand the effects of condensation on the air-side performance of heat exchangers, testing of heat exchangers under wet and dry conditions should be continued for heat exchanger geometries not tested in this study. It may be useful to study heat exchangers with greater length and more tube rows. Furthermore, the effect of contact angles on heat transfer should be studied by obtaining experimental data from heat exchangers exposed to many hours of use.
- The current model predicts the mass of retained condensate by accounting for condensate formed as droplets and as fin-tube bridges. To improve the model, other condensate geometries such as bridges that form between adjacent fins should be identified and included in the retention model. Furthermore, air-flow forces on retained condensate should be more accurately determined. Circular contact lines have been assumed for the droplets adhering to the fin surface. From the photographs of the stock fin sample this assumption is shown to be poor for larger droplets. An elliptical contact line may be used to improve the condensate retention model.

Appendix A – Data Reduction

This appendix describes the data reduction techniques and equations used for evaluating the performance of wet and dry heat exchangers. Engineering Equation Solver (EES) was used for the data reduction. Table A.1 shows the equation worksheet used for wavy-louvered heat exchangers. A parametric table was used to read in experimentally acquired parameters and to display important performance parameters. Table A.2 shows the input and output parameters used in the parametric table.

Coolant-Side

The coolant-side mass flow rate was measured with a volumetric flow meter that provided a 5 volt dc pulse with 3.092×10^5 pulses per cubic meter of liquid. Equation A.1 was used to calculate the coolant mass flow rate. The outlet coolant temperature was used to calculate the coolant density since the meter was located on the return line.

$$\dot{m}_c = 3.092x10^5 \rho_{c,out}\left(\frac{pulses}{s}\right) \tag{A.1}$$

A single-phase ethylene glycol (DOWTHERM 4000) and water mixture was circulated on the tube side of the heat exchanger. The volume fraction of glycol was determined by measuring the specific gravity of the mixture with a hydrometer. The manufacturer supplied property tables and by using the specific gravity of the mixture, property relations as shown in Table A.4 were developed.

Equation A.2 shows a correlation developed by Gnielinski [22] that was used to determine the coolant-side heat transfer coefficient, h_i. The correlation was chosen because it was applicable to the Reynolds number of this study

$$h_i = \frac{\left(f_c/8\right)\left(\mathrm{Re}_C - 1000\right)\mathrm{Pr}_c}{1 + 12.7\left(f_c/8\right)^{1/2}\left(\mathrm{Pr}_c^{2/3} - 1\right)} \cdot \frac{k_c}{D_{it}} \tag{A.2}$$

The friction factor is

$$f_c = \left(0.79\ln\left(\mathrm{Re}_C\right) - 1.64\right)^{-2} \tag{A.3}$$

where

$$\mathrm{Re}_C = \frac{\rho_c V_c D_{it}}{\mu_c} \tag{A.4}$$

and

$$\mathrm{Pr}_c = \frac{Cp_c \mu_c}{k_c} \tag{A.5}$$

Air-Side

The velocity of the air at the heat exchanger face was measured using a constant temperature thermal anemometer. As recommended by the manufacturer the velocity needed to be calibrated based on the temperature and pressure at the heat exchanger face. The calibrated velocity was calculated using Equation A.6.

$$V_{fr,cali} = \frac{V_{fr}\left(273.15 + T_{fr}\left(^\circ C\right)\right) \cdot 101.325}{294.1 P_{atm}} \tag{A.6}$$

Air properties were computed using thermophysical property functions that were built into EES.

Heat Transfer Rates

Equations A.7 through A.9 were used to calculate the heat transfer rates. Calculations were based on measurements made at the test section inlet and outlet. The data used for this study required that air-side and coolant-side heat transfer rates were within 10%.

$$q_{sens} = \dot{m}_{air} C_{Pair} (T_{in,air} - T_{out,air}) \tag{A.7}$$

$$q_{tot} = \dot{m}_{air} (h_{in,air} - h_{out,air}) \tag{A.8}$$

$$q_c = \dot{m}_c C_{Pc} (T_{out,c} - T_{in,c}) \tag{A.9}$$

Fin Efficiency

An equivalent circular area is recommended by ARI strandard 410 [18] for calculating the fin efficiency of plate-type fins. The equivalent inner radius for fins with collars touching adjacent fin is calculated using Equation A.10.

$$r_i = \frac{(D_{ot} + 2\delta)}{2} \tag{A.10}$$

The fin efficiency for the heat exchangers was determined by applying the sector method. The sector method with conduction for plain-fin heat exchangers is depicted in Figure A.1. Constant thickness hexagonal fins attached to round tubes made this method applicable. Fins are approximated by circular segments constructed by dividing each hexagonal fin into the same number of equal segments. The data reduction for this project divided each hexagonal fin into 8 zones. Each zone was then divided into 4 sectors. After the length of the edges of each zone is approximated, the radius ratio, R_n, and the surface

area, S_n, of each sector can be calculated. Equation A.11 and Equation A.12 are used to calculate the radius ratio and surface area for sectors with constant edge M or zones 2,3,6, and 7.

$$R_n = \frac{M}{r_{if}}\sqrt{\left(\frac{2n-1}{2N}\right)^2 + \left(\frac{L}{M}\right)^2} \tag{A.11}$$

$$S_n = \frac{r_{if}^2}{2}\left(R_n^2 - 1\right)\left[\tan^{-1}\left(\frac{nM}{NL}\right) - \tan^{-1}\left(\frac{(n-1)M}{NL}\right)\right] \tag{A.12}$$

where n = 1, 2, 3 ... N is the number of sectors in each zone.

where

$$M = \frac{S_t}{2} \tag{A.13}$$

and

$$L = \frac{S_l}{2} \tag{A.14}$$

Equation A.15 and Equation A.16 are used to calculate the radius ratio and surface area for sectors with constant edge L or zones 1, 4, 5, and 8.

$$R_n = \frac{M}{r_{if}}\sqrt{\left(\frac{2n-1}{2N}\right)^2\left(\frac{L}{M}\right)^2 + 1} \tag{A.15}$$

$$S_n = \frac{r_{if}^2}{2}\left(R_n^2 - 1\right)\left[\tan^{-1}\left(\frac{nL}{NM}\right) - \tan^{-1}\left(\frac{(n-1)L}{NM}\right)\right] \tag{A.16}$$

After determining the radius ratio, the Hong and Webb [22] equation is used to determine the fin efficiency. Hong and Webb modified the Schmidt [23] equation for fin efficiency of a circular fin with a round tube to cover a wider range.

$$\phi = \frac{\tanh(mH')\cos(0.1mH')}{mH'} \tag{A.17}$$

where

$$m = \left(\frac{2h}{\kappa_t \delta_f}\right)^{1/2} \tag{A.18}$$

and

$$H' = r_i(r_n - 1)(1 + 0.35\ln R_n) \tag{A.19}$$

The fin efficiency of each sector is calculated and then with the surface area of each sector, the fin efficiency is then determined by applying Equation A.20.

$$\phi = \frac{\sum_{n=1}^{N_s} \phi_n S_n}{\sum_{n=1}^{N_s} S_n} \tag{A.20}$$

where N_s is the number of sectors in each zone.

Figure A.2 shows the sector method with conduction for determining fin efficiency for constant thickness hexagonal louvered fins. The technique uses similar calculations to find the fin efficiency of a plain fin. The only difference is that the radius ratio has been modified for a better approximation. Equation A.21 is applied to find radius ratio for sectors with constant M edge.

$$R_n = \frac{\left(M_s\sqrt{\left(\frac{2n-1}{2N}\right)^2\left(\frac{L_s}{M_s}\right)^2}\right) + h_l}{r_i} \tag{A.21}$$

This radius ratio calculation was modified from the plain fin equation by replacing M with M_s and L with L_s. These two values were measured directly. The height of the

louvers h_l was added to the sectors with constant M_s. The equations used to find surface area and the radius ratio for sectors with constant L edge remained unchanged.

Air-Side Heat Transfer Coefficient

The surface temperature was compared to the dewpoint of the air to determine if the heat exchangers were wet or dry. If the surface temperature was greater than the dewpoint the dry air-side heat transfer coefficient was used. However, if the surface temperature was found to be lower than the dewpoint of the air, then an effective air-side heat transfer coefficient for wet conditions must be determined.

$$R_a = \frac{1}{\eta_o h_{eff} A_{tot}} \tag{A.22}$$

By knowing the fin efficiency, the air-side heat transfer coefficient is determined by iterating the data reduction equations.

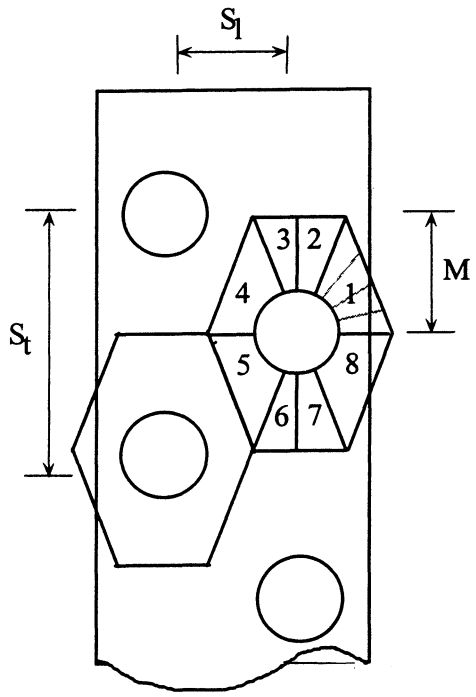

Figure A.1: Sector method with conduction for determining fin efficiency for constant thickness hexagonal plain fin

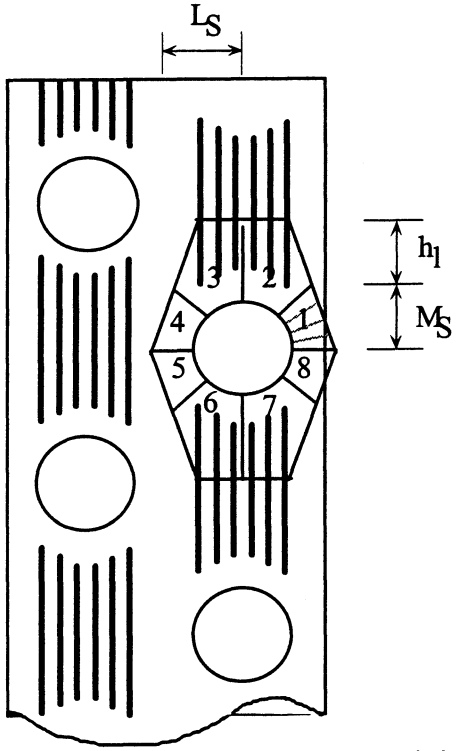

Figure A.2: Sector method with conduction for determining fin efficiency for constant thickness hexagonal louvered fin

Table A.1 Engineering equation solver worksheet used for wavy-louvered exchangers

```
PROCEDURE HUM1(Tdp_inC: P_sat1, W1)

C8=-5.8002206*10^3
C9=-5.516256
C10=-4.8640239*10^(-2)
C11=4.1764768*10^(-5)
C12=-1.4452093*10^(-8)
C13=6.5459673

C1=-5.9745359*10^3
C2=-5.1523058*10^(-1)
C3=-9.677843*10^(-3)
C4=6.2215701*10^(-7)
C5=2.0747825*10^(-9)
C6=-9.484024*10^(-13)
C7=4.1635019

IF (Tdp_inC>0) THEN

    Tdp_inK:=Tdp_inC+273.15

P_sat1:=Exp(C8/Tdp_inK+C9+C10*Tdp_inK+C11*(Tdp_inK)^2+C12*(Tdp_inK)^3+C13*ln(Tdp_inK))
    w1:=0.62188*P_sat1/(101.325-P_sat1)

    ELSE
    Tdp_inK:=Tdp_inC+273.15

P_sat1:=Exp(C1/Tdp_inK+C2+C3*Tdp_inK+C4*(Tdp_inK)^2+C5*(Tdp_inK)^3+C6*(Tdp_inK)^4+C7*
ln(Tdp_inK))
    w1:=0.62188*P_sat1/(101.325-P_sat1)

ENDIF

END


PROCEDURE HUMAIR1(Tin_air: P_air1, W_air1)

C8=-5.8002206*10^3
C9=-5.516256
C10=-4.8640239*10^(-2)
C11=4.1764768*10^(-5)
C12=-1.4452093*10^(-8)
C13=6.5459673

C1=-5.9745359*10^3
C2=-5.1523058*10^(-1)
C3=-9.677843*10^(-3)
C4=6.2215701*10^(-7)
C5=2.0747825*10^(-9)
C6=-9.484024*10^(-13)
```

Table A.1 (cont.)

```
C7=4.1635019

IF (Tin_air>0) THEN

     Tin_airK:=Tin_air+273.15
     P_air1:=Exp(C8/ Tin_airK+C9+C10* Tin_airK+C11*( Tin_airK)^2+C12*( Tin_airK)^3+C13*ln(
Tin_airK))
     W_air1:=0.62188*P_air1/(101.325-P_air1)

     ELSE
     Tin_airK:=Tin_airC+273.15
     P_air1:=Exp(C1/ Tin_airK+C2+C3* Tin_airK+C4*( Tin_airK)^2+C5*( Tin_airK)^3+C6*(
Tin_airK)^4+C7*ln( Tin_airK))
     W_air1:=0.62188*P_air1/(101.325-P_air1)

ENDIF

END

PROCEDURE HUM2(Tdp_outC: P_sat2, w2)

C8=-5.8002206*10^3
C9=-5.516256
C10=-4.8640239*10^(-2)
C11=4.1764768*10^(-5)
C12=-1.4452093*10^(-8)
C13=6.5459673

C1=-5.9745359*10^3
C2=-5.1523058*10^(-1)
C3=-9.677843*10^(-3)
C4=6.2215701*10^(-7)
C5=2.0747825*10^(-9)
C6=-9.484024*10^(-13)
C7=4.1635019

IF (Tdp_outC>0) THEN

     Tdp_outK:=Tdp_outC+273.15

P_sat2:=Exp(C8/Tdp_outK+C9+C10*Tdp_outK+C11*(Tdp_outK)^2+C12*(Tdp_outK)^3+C13*ln(Tdp_
outK))
     w2:=0.62188*P_sat2/(101.325-P_sat2)

     ELSE
     Tdp_outK:=Tdp_outC+273.15

P_sat2:=Exp(C1/Tdp_outK+C2+C3*Tdp_outK+C4*(Tdp_outK)^2+C5*(Tdp_outK)^3+C6*(Tdp_outK)^
4+C7*ln(Tdp_outK))
     w2:=0.62188*P_sat2/(101.325-P_sat2)
```

Table A.1 (cont.)

```
ENDIF

END


PROCEDURE HUMAIR2(Tout_air: P_air2, W_air2)

C8=-5.8002206*10^3
C9=-5.516256
C10=-4.8640239*10^(-2)
C11=4.1764768*10^(-5)
C12=-1.4452093*10^(-8)
C13=6.5459673

C1=-5.9745359*10^3
C2=-5.1523058*10^(-1)
C3=-9.677843*10^(-3)
C4=6.2215701*10^(-7)
C5=2.0747825*10^(-9)
C6=-9.484024*10^(-13)
C7=4.1635019

IF (Tout_air>0) THEN

    Tout_airK:=Tout_air+273.15
    P_air2:=Exp(C8/ Tout_airK+C9+C10* Tout_airK+C11*( Tout_airK)^2+C12*(
Tout_airK)^3+C13*ln( Tout_airK))
    W_air2:=0.62188*P_air2/(101.325-P_air2)

    ELSE
    Tout_airK:=Tout_airC+273.15
    P_air2:=Exp(C1/ Tout_airK+C2+C3* Tout_airK+C4*( Tout_airK)^2+C5*( Tout_airK)^3+C6*(
Tout_airK)^4+C7*ln( Tout_airK))
    W_air2:=0.62188*P_air2/(101.325-P_air2)

ENDIF

END

PROCEDURE HUMSAT1(Tsin: P_s1, ws1)

C8=-5.8002206*10^3
C9=-5.516256
C10=-4.8640239*10^(-2)
C11=4.1764768*10^(-5)
C12=-1.4452093*10^(-8)
C13=6.5459673
```

Table A.1 (cont.)

```
C1=-5.9745359*10^3
C2=-5.1523058*10^(-1)
C3=-9.677843*10^(-3)
C4=6.2215701*10^(-7)
C5=2.0747825*10^(-9)
C6=-9.484024*10^(-13)
C7=4.1635019

IF (Tsin>0) THEN

    TsinK:=Tsin+273.15
    P_s1:=Exp(C8/TsinK+C9+C10*TsinK+C11*(TsinK)^2+C12*(TsinK)^3+C13*ln(TsinK))
    ws1:=0.62188*P_s1/(101.325-P_s1)

    ELSE
    TsinK:=Tsin+273.15
    P_s1:=Exp(C1/TsinK+C2+C3*TsinK+C4*(TsinK)^2+C5*(TsinK)^3+C6*(TsinK)^4+C7*ln(TsinK))
    ws1:=0.62188*P_s1/(101.325-P_s1)

ENDIF

END

PROCEDURE HUMSAT2(Tsout: P_s2, ws2)

C8=-5.8002206*10^3
C9=-5.516256
C10=-4.8640239*10^(-2)
C11=4.1764768*10^(-5)
C12=-1.4452093*10^(-8)
C13=6.5459673

C1=-5.9745359*10^3
C2=-5.1523058*10^(-1)
C3=-9.677843*10^(-3)
C4=6.2215701*10^(-7)
C5=2.0747825*10^(-9)
C6=-9.484024*10^(-13)
C7=4.1635019

IF (Tsout>0) THEN

    TsoutK:=Tsout+273.15
    P_s2:=Exp(C8/TsoutK+C9+C10*TsoutK+C11*(TsoutK)^2+C12*(TsoutK)^3+C13*ln(TsoutK))
    ws2:=0.62188*P_s2/(101.325-P_s2)

    ELSE
    TsoutK:=Tsout+273.15
```

Table A.1 (cont.)

```
P_s2:=Exp(C1/TsoutK+C2+C3*TsoutK+C4*(TsoutK)^2+C5*(TsoutK)^3+C6*(TsoutK)^4+C7*ln(Tsout
K))
    ws2:=0.62188*P_s2/(101.325-P_s2)

ENDIF

END

PROCEDURE HUMCAL(Tout_calc: P_calc, wout_calc)

C8=-5.8002206*10^3
C9=-5.516256
C10=-4.8640239*10^(-2)
C11=4.1764768*10^(-5)
C12=-1.4452093*10^(-8)
C13=6.5459673

C1=-5.9745359*10^3
C2=-5.1523058*10^(-1)
C3=-9.677843*10^(-3)
C4=6.2215701*10^(-7)
C5=2.0747825*10^(-9)
C6=-9.484024*10^(-13)
C7=4.1635019

IF (Tout_calc>0) THEN

    Tout_calcK:=Tout_calc+273.15

P_calc:=Exp(C8/Tout_calcK+C9+C10*Tout_calcK+C11*(Tout_calcK)^2+C12*(Tout_calcK)^3+C13*ln(
Tout_calcK))
    wout_calc:=0.62188*P_calc/(101.325-P_calc)

    ELSE
    Tout_calcK:=Tout_calc+273.15

P_calc:=Exp(C1/Tout_calcK+C2+C3*Tout_calcK+C4*(Tout_calcK)^2+C5*(Tout_calcK)^3+C6*(Tout_c
alcK)^4+C7*ln(Tout_calcK))
    wout_calc:=0.62188*P_calc/(101.325-P_calc)

ENDIF

END

"11 Input parameters from table:
T_fr, Tin_air,Tout_air,Tdp_inF,Tdp_outF,Tin_c,Tout_c,R_c,fpi,DelP_air,V_fr"

"Geometry"
Hf=8*Convert(in,m)                    {Height of fin, m}
W=12*Convert(in,m)                    {Width of HX, m}
Lf=1.737*Convert(in,m)                {Length of Fin, m}
```

Table A.1 (cont.)

```
D_coll=D_ot+2*delta                                  {Diameter of collar, m}
L_t=W*Nt                                             {Tube Length, m}
D_it=(0.371-0.031*2)*Convert(in,m)                   {Inside diameter of tube, m}
D_ot=(0.371)*Convert(in,m)                           {Outside diameter of tube, m}
delta=.0045*Convert(in,m)                            {Fin Thickness, m}
Nf=fpi*12                                            {Number of Fins given fpi}
Nfs=Nf*2-1                                           {Number of Fin Surfaces}
Nt=16                                                {Number of Tubes}
fp=(1/fpi)*Convert(in,m) - delta                     {fin pitch}

"Area Calcs"
A_fr=Hf*W                                            {Frontial Area, m^2}
A_min=A_fr-(delta*Hf*Nf)-(8*D_ot*(W-Nf*delta))       {Minimum free flow area, m^2}

Afs=(Hf*Lf)-(Nt*(D_ot+2*delta)^2)*(pi/4)             {Area per fin surface, m^2}
Atr=(W-Nf*delta)*pi*(D_coll)                         {Area per tube row, m^2}
Af=Nfs*Afs                                           {Total fin area, m^2}
At=Nt*Atr                                            {Total tube Area  m^2}
A_tot=Af+At                                          {A_tot=Af+At  m^2}
A_i=pi*D_it*L_t

"Coolant Side"
Tin_cF=Tin_c*1.8+32
Tout_cF=Tout_c*1.8+32

A_ct=(D_it)^2/4*pi                                   {Cross Section Area of Tube, m^2}
Q_c=R_c/10/1170.54*0.003785                          {Volumetric Flow Rate of Coolant, m^3/s}
V_c=Q_c/A_ct
m_c=Q_c*Rho_c                                        {Kg/s}

"Colant Properties, 32.6% Concentration"
{Density of Coolant, Kg/m^3}
Rho_c=(((-0.361004E-07)*(Tout_cF)^3)-((0.281889E-04)*(Tout_cF)^2)-(0.0127283*Tout_cF)+67.0996)/0.06243
{Viscosity of Coolant, Ns/m^2}
Vis_c=(((-0.980059E-05)*(Tin_cF)^3)+((0.232579E-02)*(Tin_cF)^2)-(0.216794*Tin_cF)+9.47314)*(1E-03)
{Conductivity of Coolant, W/mK}
k_c=(((-0.207510E-07)*(Tin_cF)^3)+((0.251828E-05)*(Tin_cF)^2)+(0.289039E-
03*Tin_cF)+0.231444)/0.5778/1000
{Specific Heat of Coolant, KJ/KgK}
Cp_c=(((-0.272010E-07)*(Tin_cF)^3)+((0.370036E-05)*(Tin_cF)^2)+(0.259944E-03*Tin_cF)+
        0.829350)/(2.389E-04)/1000

"Coolant-Side Heat Transfer Coefficient; Gnielinski correlation"
Re_c=(Rho_c*V_c*D_it)/Vis_c                           {based on inside tube diameter}
f_c=(0.79*ln((Re_c))-1.64)^(-2)                      {Friction Factor of Coolant}
Pr_c=Cp_c*Vis_c/k_c
Nu_c=((f_c/8)*((Re_c)-1000)*Pr_c)/(1+12.7*((f_c/8)^0.5)*(((Pr_c)^(2/3))-1))
h_i=Nu_c*k_c/(D_it)                                  {KW/m^2-K Tube Side Heat Transfer Coefficient}
```

Table A.1 (cont.)

```
"Air Side"
Tdp_inC=(Tdp_inF-32)/1.8
Tdp_outC=(Tdp_outF-32)/1.8

CALL HUM1(Tdp_inC:P_sat1, w1)
CALL HUMAIR1(Tin_air:P_air1, W_air1)
CALL HUM2(Tdp_outC:P_sat2, w2)
CALL HUMAIR2(Tout_air:P_air2, W_air2)

RH_in=P_sat1/P_air1
RH_out=P_sat2/P_air2

T_mair=(Tin_air+Tout_air)/2                                   {Mean Air Temp}
w_mair=(w1+w2)/2                                              {Mean Humidity Ratio}

"Air Properties"
Rho_air=Density(AirH2O,T=T_mair,P=101.325,w=w_mair)           {Kg/m^3}
Vis_air=Viscosity(AirH2O,T=T_mair,P=101.325,w=w_mair)         {Ns/m^2}
k_air=Conductivity(AirH2O,T=T_mair,P=101.325,w=w_mair)/1000   {KW/mK}
Cpin_air=1.006+1.845*w1                                       {KJ/KgK}
Cpout_air=1.006+1.845*w2                                      {KJ/KgK}
Cp_mair=(Cpin_air+Cpout_air)/2
hin_air=Enthalpy(AirH2O,T=Tin_air,P=101.325,w=w1)             {KJ/Kg}
hout_air=Enthalpy(AirH2O,T=Tout_air,P=101.325,w=w2)           {KJ/Kg}
V_adj=V_fr*(273.15+Tin_air)/(273.15+T_fr)                     {Air Velocity Calibration}

m_dot_air=V_adj*Rho_air*A_fr
V_max=V_adj*(A_fr/A_min) * (Density (AirH2O,T=Tin_air,P=101.325,w=w1) / Rho_air)

"Heat Transfer Rate"
q_ref=m_c * Cp_c*(Tout_c-Tin_c)
q_sens=m_dot_air*Cp_mair*(Tin_air-Tout_air)                   {KW}
q_tot=m_dot_air*(hin_air-hout_air)                            {KW}

q_ave=(q_tot+q_ref)/2
q_error=(q_ref-q_ave)/q_ave*100

"Fin Efficiency Calculation"
Ts_m=(Tsin+Tsout)/2

Ms=0.013825
Ls=0.00735

WD=Ms
LN=Ls

Kt=0.3387                                                     {Kw/m-C, ARI410, C122000}
hfg=2501
D_AB=0.26E-4                                                  {Binary mass diffusion coefficient}
Le=k_air/(Rho_air*Cp_mair*D_AB)
```

Table A.1 (cont.)

```
"Sector method with conduction"
m2=(2*h_eff/Kt/delta)^0.5
r_if=(D_ot+2*delta)/2                {equivalent inner radius for fins with collars touching adjacent fin}
Nsectors=4

Duplicate n=1, Nsectors
"Octans 1 , 4, 5 and 8"
    R[n]=(WD/r_if)*(((((2*n-1)/(2*Nsectors))^2)+(LN/WD)^2))^0.5
    S[n]=(r_if^2)/2*((R[n]^2)-1)*(arctan(n*WD/Nsectors/LN)-arctan((n-1)*WD/Nsectors/LN))*pi/180
    Rho[n]=(R[n]-1)*(1+0.35*ln(R[n]))
    H[n]=r_if*Rho[n]
    Eff[n]=tanh(m2*H[n])*cos(0.1*m2*H[n])/(m2*H[n])
    Num[n]=4*Eff[n]*S[n]
    Den[n]=4*S[n]
"Octans 2 ,3,6 and 7"
    R[2*Nsectors+1-n]=(WD/r_if)*(((((2*n-1)/(2*Nsectors))^2)*(LN/WD)^2)+1)^0.5
    S[2*Nsectors+1-n]=(r_if^2)/2*((R[2*n+1-n]^2)-1)*(arctan(n*LN/Nsectors/WD)-
      arctan((n-1)*LN/Nsectors/WD))*pi/180
    Rho[2*Nsectors+1-n]=(R[2*Nsectors+1-n]-1)*(1+0.35*ln(R[2*Nsectors+1-n]))
    H[2*Nsectors+1-n]=r_if*Rho[2*Nsectors+1-n]
    Eff[2*Nsectors+1-n]=tanh(m2*H[2*Nsectors+1-n])*
      cos(0.1*m2*H[2*Nsectors+1-n])/(m2*H[2*Nsectors+1-n])
    Num[2*Nsectors+1-n]=4*Eff[2*Nsectors+1-n]*S[2*Nsectors+1-n]
    Den[2*Nsectors+1-n]=4*S[2*Nsectors+1-n]
End

Num=SUM(Num[n], n=1,Nsectors)+SUM(Num[2*Nsectors+1-n], n=1, Nsectors)
Den=SUM(Den[n], n=1,Nsectors)+SUM(Den[2*Nsectors+1-n], n=1, Nsectors)

Phi=Num/Den
Eta=(Phi*Af+At)/A_tot
R_a=1/(Eta*h_eff*A_tot)
R_t=ln(D_ot/D_it)/2/pi/Kt/L_t
R_m=R_t+R_a
R_i=1/h_i/A_I

"Heat Transfer Coefficient Calculation"
C1=(R_m+R_i)/Cp_mair*hwet*A_tot
C1*(hin_air-hs1)=Tsin-Tin_c

CALL HUMSAT1(Tsin:P_s1,ws1)
CALL HUMSAT2(Tsout:P_s2,ws2)

hs1=Enthalpy(AirH2O,T=Tsin,P=101.325,w=ws1)
hs2=Enthalpy(AirH2O,T=Tsout,P=101.325,w=ws2)
hh1=((hin_air-hs1)-(hout_air-hs2))/lmhd
hin_air=(exp(hh1))*(hout_air-hs2)+hs1
tt1=((Tin_air-Tout_c)-(Tout_air-Tin_c))/lmtd
Tin_air=(exp(tt1))*(Tout_air-Tin_c)+Tout_c
```

Table A.1 (cont.)

```
qsens_calc=hwet*A_tot*lmtd
Tout_calc=Tin_air-(qsens_calc/m_air/Cp_mair)
CALL HUMCAL(Tout_calc: P_calc, wout_calc)
hout_air=Enthalpy(AirH2O,T=Tout_calc,P=101.325,w=wout_calc)
RH2_calc=RelHum(AirH2O,T=Tout_calc,P=101.325,w=wout_calc)

q_tot=A_tot*lmhd/Cp_mair*hwet

R1=(w1-ws1)*(1/Le^(2/3)-1)*hfg/(hin_air-hs1)
R2=(w2-ws2)*(1/Le^(2/3)-1)*hfg/(hout_air-hs2)

b1=(hin_air-hs1)/Cp_mair/(Tin_air-Tsin)-1
b2=(hout_air-hs2)/Cp_mair/(Tout_air-Tsout)-1

"j & f factor"
Rho_airavg=(Density(AirH2O,T=Tin_air,P=101.325,w=w1)+Density(AirH2O,T=Tout_air,P=101.325,w=
w2))/2
Rho_air12=(Density(AirH2O,T=Tin_air,P=101.325,w=w1)/Density(AirH2O,T=Tout_air,P=101.325,w=w
2))
Rho_aira1=Rho_airavg/Density(AirH2O,T=Tout_air,P=101.325,w=w2)
DelP_airN=DelP_air*249.08891                                    {N/m^2}
Area_mt=A_min/A_tot
Area_mf=A_min/A_fr
Dh=4*A_min*Lf/A_tot

m_air=V_fr*Rho_air*A_fr
G_air=V_max*Rho_air
Re_Dh=G_air*Dh/Vis_air
Re_coll=G_air*D_coll/Vis_air

Pr_air=Cp_mair*Vis_air/k_air
St_air=Nu_Dcoll/(Re_D_coll*Pr_air)
Nu_Dcoll=hwet*D_coll/k_air

f=((2*DelP_airN*Rho_air)/(G_air)^2 )*Area_mt-(1+(Area_mf)^2 )*( Rho_air12-1 )*Area_mt*Rho_aira1
j=St_air*(Pr_air)^(2/3)
```

Table A.2 Input and output parameters used in the engineering equation solver (EES) parametric table.

Input Parameters	
Parameter	**Definition**
fpi	Fins per inch
V_{fr}	Air-flow face velocity (m/s)
T_{fr}	Air-flow face temperature (°C)
$T_{in,\ air}$	Air inlet temperature (°C)
$T_{out,\ air}$	Air outlet temperature (°C)
$T_{dp,\ in}$	Inlet dewpoint temperature (°F)
$T_{dp,\ out}$	Outlet dewpoint temperature (°F)
$T_{in,\ c}$	Coolant inlet temperature (°C)
$T_{out,\ c}$	Coolant outlet temperature (°C)
$DelP_{air}$	Pressure drop across heat exchanger (in H_2O)
R_c	Coolant flow rate (pulses/10s)
Output Parameters	
q_{err}	Energy balance
V_{max}	Velocity based on minimum free flow area
Re_{Dcoll}	Reynolds number based on collar diameter
Re_{Dh}	Reynolds number based on hydraulic diameter
Re_c	Coolant Reynolds number based on inner diameter
f	Friction factor
j	Sensible j factor
Nu_{Dcoll}	Nusselt number based on collar diameter
Nu_{Dh}	Nusselt number based on hydraulic diameter
h	Air-side heat transfer coefficient (KW/m^2K)
h_i	Coolant-side heat transfer coefficient (KW/m^2K)

Table A.3 Definitions of calculated parameter

Parameter	Definition
G_{air}	$V_{\max}\rho_{air}$
$V_{\max}$	$V_{air}\left(\frac{A_{fr}}{A_{\min}}\right)\left(\frac{\rho_{air,in}}{\rho_{air}}\right)$
Re_{Dh}	$\frac{G_{air}D_h}{\mu_{air}}$
Re_{Dcoll}	$\frac{G_{air}D_{coll}}{\mu_{air}}$
Nu_{Dcoll}	$\frac{hD_{coll}}{\kappa_{air}}$
j	$StPr^{2/3}$
St	$\frac{Nu}{RePr}=\frac{h}{G_{air}Cp_{mair}}$
Pr_{air}	$\frac{Cp_{mair}\mu_{air}}{\kappa_{air}}$
Pr_c	$\frac{Cp_c\mu_c}{\kappa_c}$
Le	$\frac{Sc}{pr}=\frac{\kappa_{air}}{\rho_{air}C_{P_{mair}}D_{AB}}$
f	$\frac{2\Delta P_{HX}\rho_{air}}{G_{air}^2}\left(\frac{A_{\min}}{A_{tot}}\right)-\left(1+\sigma^2\right)\left(\frac{\rho_{air,in}}{\rho_{air,out}}-1\right)\left(\frac{A_{\min}}{A_{tot}}\right)\left(\frac{\rho_{air}}{\rho_{air,in}}\right)$

Table A.4 Coolant property evaluations

Property	Relation
$k_c\left(\frac{W}{m\cdot K}\right)$	$\frac{0.2314+2.89\text{x}10^{-4}(T_c(°F))+2.518\text{x}10^{-6}(T_c(°F))^2-2.075x10^{-8}(T_c(°F))^3}{0.5778}$
$\rho_c\left(\frac{kg}{m^3}\right)$	$\frac{\left(67.099-1.273x10^{-2}T_c(°F)-2.819\text{x}10^{-5}(T_c(°F))^2-3.610\text{x}10^{-8}(T_c(°F))^3\right)}{0.06243}$
$\mu_c\left(\frac{N\cdot s}{m^2}\right)$	$9.473\text{x}10^{-3}-2.167\text{x}10^{-4}(T_c(°F))+2.326\text{x}10^{-6}(T_c(°F))^2-9.80\text{x}10^{-9}(T_c(°F))^3$
$Cp_c\left(\frac{kJ}{kg\cdot K}\right)$	$\frac{0.8293+2.599\text{x}10^{-4}(T_c(°C))+3.700\text{x}10^{-6}(T_c(°C))^2-2.720\text{x}10^{-8}(T_c(°C))^3}{0.2389}$

Appendix B – Buckingham Pi Analysis

The Buckingham Pi theorem was used in finding the independent parameters for the sensible j and f factor correlations. The theorem determines the relationship between a function expressed in dimensional parameters and a related function expressed in nondimensional parameters. By using the Buckingham Pi theorem the determination of the nondimensional parameters are found quickly and easily.

Determining the $\prod$ Groups

The determination of the dimensionless groups used to correlate the j and f data can be found by following a six step procedure as outlined by Fox and McDonald [25].

1. Determine all the geometric and flow parameters involved in the phenomenon.
2. Select a set of fundamental dimensions. (mass, length, time, etc).
3. Express the parameters in terms of the fundamental dimensions.
4. Choose a set of repeating parameters from the whole set of parameters. The number of repeating parameters used should equal the number of fundamental dimensions. Furthermore, no repeating parameters can have the same net dimensions differing only be a single exponent. Finally be sure that the repeating parameters includes all of the fundamental dimensions.
5. Form dimensionless groups by setting up dimensional equations. Combine the repeating parameters from step 4 with all the other parameters.
6. Using the fundamental dimensions, verify that the dimensionless groups are indeed dimensionless.

Dimensional Analysis for j Factor

To determine the nondimensional variables involved in the j factor correlation, the dimensions and air-side properties found in Equation B.1 were used. A total of 15 variables were used.

$$q = f\left(H, W, L, S_l, S_t, f_s, \delta_f, D_{coll}, k_{air}, \mu_{air}, \rho_{air}, C_{p,air}, \dot{m}, \Delta T\right) \tag{B.1}$$

A set of four fundamental dimensions were used: mass, length, time, and temperature. Setting up dimensional equations, we obtain the following 11 dimensionless groups:

$$\Pi_1 = \frac{H}{D_{coll}} \qquad \Pi_2 = \frac{W}{D_{coll}} \qquad \Pi_3 = \frac{L}{D_{coll}} \qquad \Pi_4 = \frac{S_l}{D_{coll}}$$

$$\Pi_5 = \frac{S_t}{D_{coll}} \qquad \Pi_6 = \frac{f_s}{D_{coll}} \qquad \Pi_7 = \frac{\delta_f}{D_{coll}} \qquad \Pi_8 = \frac{\kappa_{air}}{C_{p,air}\mu_{air}}$$

$$\Pi_9 = \frac{\dot{m}}{D_{coll}\mu_{air}} \qquad \Pi_{10} = \frac{D_{coll}^2 C_{p,air}\rho^2 \Delta T}{\mu_{air}^2} \qquad \Pi_{11} = \frac{D_{coll}\rho_{air}^2 q}{\mu_{air}^3}$$

The functional relationship is then given by Equation B.2.

$$\Pi_{11} = f(\Pi_1, \Pi_2, \Pi_3, \Pi_4, \Pi_5, \Pi_6, \Pi_7, \Pi_8, \Pi_9, \Pi_{10}) \tag{B.2}$$

Each dimensionless group can be expressed as a product of itself with another dimensionless group and with some algebraic manipulation well known nondimensional numbers were found.

$$\Pi_8 = \frac{\kappa_{air}}{C_{p,air}\mu_{air}} = Pr$$

since $\dot{m} = \rho_{air} V_{air} HW$

$$\Pi_9 = \frac{\dot{m}}{D_{coll}\mu_{air}} \cdot \frac{D_{coll}}{H} \cdot \frac{D_{coll}}{W} = \frac{V_{air} D_{coll} \rho_{air}}{\mu_{air}} = Re_{Dcoll}$$

$$\Pi_{10} = \frac{D_{coll}^2 C_{p,air} \rho^2 \Delta T}{\mu_{air}^2} \cdot \left(\frac{\mu_{air}}{V_{air} D_{coll} \rho_{air}} \right)^2 = \frac{1}{Ec}$$

similarly by using $q = hA\Delta T$

$$\Pi_{11} = \frac{D_{coll} \rho_{air}^2 q}{\mu_{air}^3} = Nu_{Dcoll}$$

Equation B.3 shows the simplified functional relationship.

$$Nu_{Dcoll} = f\left(\frac{H}{D_{coll}}, \frac{W}{D_{coll}}, \frac{L}{D_{coll}}, \frac{S_l}{D_{coll}}, \frac{S_t}{D_{coll}}, \frac{f_s}{D_{coll}}, \frac{\delta_f}{D_{coll}}, Pr, Re_{Dcoll}, Ec\right) \quad \text{(B.3)}$$

By using the relationship between the Nusselt number and the sensible j factor

$$j = \frac{Nu}{RePr^{1/3}} \quad \text{(B.4)}$$

the j factor can be expressed as shown in Equation B.5

$$j = f\left(\frac{H}{D_{coll}}, \frac{W}{D_{coll}}, \frac{L}{D_{coll}}, \frac{S_l}{D_{coll}}, \frac{S_t}{D_{coll}}, \frac{f_s}{D_{coll}}, \frac{\delta_f}{D_{coll}}, Re_{Dcoll}, Ec\right) \quad \text{(B.5)}$$

For the heat exchangers studied in this project many of the geometric parameters were constant. If the Eckert number and constant dimensionless groups are neglected the functional relationship for j factor is shown in Equation B.6.

$$j = f\left(\frac{f_s}{D_{eoll}}, Re_{Dcoll}\right) \quad \text{(B.6)}$$

The proposed j factor correlation is then shown below in Equation B.7.

$$j = C\left(Re_{Dcoll}\right)^a \left(\frac{f_s}{D_{coll}}\right)^b \quad \text{(B.7)}$$

where C, a, and b are constants which may be determined by performing a regression on the dimensionless variables.

Dimensional Analysis for f Factor

In determining the nondimensional variables involved in the f factor correlation, the dimensions and air-side properties found in Equation B.8 were used. A total of 12 variables were used.

$$\Delta p = f\left(H, W, L, S_l, S_t, f_s, \delta_f, D_c, \mu_{air}, \rho_{air}, \dot{m}\right) \tag{B.8}$$

Similar to the j factor analysis a set of three fundamental dimensions were used: mass, length, and time. Setting up dimensional equations, we obtain the following 9 dimensionless groups:

$$\Pi_1 = \frac{H}{D_{coll}} \qquad \Pi_2 = \frac{W}{D_{coll}} \qquad \Pi_3 = \frac{L}{D_{coll}}$$

$$\Pi_4 = \frac{S_l}{D_{coll}} \qquad \Pi_5 = \frac{S_t}{D_{coll}} \qquad \Pi_6 = \frac{f_s}{D_{coll}}$$

$$\Pi_7 = \frac{\delta_f}{D_{coll}} \qquad \Pi_8 = \frac{\mu_{air} D_{coll}}{\dot{m}} \qquad \Pi_9 = \frac{\Delta p D_{coll}^4 \rho_{air}}{\dot{m}^2}$$

The functional relationship is shown in Equation B.9.

$$\Pi_9 = f(\Pi_1, \Pi_2, \Pi_3, \Pi_4, \Pi_5, \Pi_6, \Pi_7, \Pi_8) \tag{B.9}$$

or

$$\frac{\Delta p D_{coll}^4 \rho_{air}}{\dot{m}^2} = f\left(\frac{H}{D_{coll}}, \frac{W}{D_{coll}}, \frac{L}{D_{coll}}, \frac{S_l}{D_{coll}}, \frac{S_t}{D_{coll}}, \frac{f_s}{D_{coll}}, \frac{\delta_f}{D_{coll}}, \frac{\mu_{air} D_{coll}}{\dot{m}}\right) \tag{B.10}$$

With some algebraic manipulation this can be rewritten as shown in Equation B.11.

$$f = f(\frac{H}{D_{coll}}, \frac{W}{D_{coll}}, \frac{L}{D_{coll}}, \frac{S_l}{D_{coll}}, \frac{S_t}{D_{coll}}, \frac{f_s}{D_{coll}}, \frac{\delta_f}{D_{coll}}, Re_{Dcoll}) \quad \text{(B.11)}$$

If the constant dimensionless groups are neglected the functional relationship for f factor is shown in Equation B.12.

$$f = f(\frac{f_s}{D_{eoll}}, Re_{Dcoll}) \quad \text{(B.12)}$$

The proposed j factor correlation is then shown below in Equation B.13.

$$f = C(Re_{Dcoll})^a \left(\frac{f_s}{D_{coll}}\right)^b \quad \text{(B.13)}$$

where C, a, and b are constants.

Appendix C – Uncertainty Analysis

Uncertainties in the experimentally measured and reduced data are discussed in this appendix. The errors in the measured parameters are discussed and propagated to estimate the uncertainties in the calculated parameters.

Uncertainty in Measured Parameters

The errors associated with the various experimental measurements are shown in Table C.1. The dewpoint of the air was measured by chilled mirror hygrometers and had a measurement uncertainty of ±0.2°C. Coolant flow rate was measured using an oscillating piston type flow meter with a measurement uncertainty of ±0.5%. Air-flow velocities were measured using a constant temperature thermal anemometer with a calibrated uncertainty of ±1%. An electric manometer with an uncertainty of ±.0.124 Pa was used to measure the air-side pressure drop across the heat exchanger. Type-T thermocouples were used to measure the air temperature and the coolant temperature. Each thermocouple was individually referenced to a thermocouple located in an ice bath and calibrated to a NIST traceable mercury-in-glass thermometer. Calibration data were fit with fifth order polynomials for each thermocouple. The uncertainty associated with the thermocouples was ±0.3°C.

Uncertainty in Calculated Values

The uncertainties in calculated experimental values were determined using techniques by Kline and McClintock [26]. The propagation of error through the measured

values introduces an uncertainty in calculated parameters. Equation C.1 was used to determine the uncertainties in the calculated values.

$$W_X = \left[\left(\frac{\partial X}{\partial Y_1} W_1 \right)^2 + \left(\frac{\partial X}{\partial Y_2} W_2 \right)^2 + \ldots + \left(\frac{\partial X}{\partial Y_n} W_n \right)^2 \right]^{1/2} \quad \text{(C.1)}$$

Where W_n = uncertainty of variable n, n=1,2,3,…,n

W_X = propagating uncertainty in result

$\frac{\partial X}{\partial Y_n}$ = partial derivative of result with respect to variable, n

Uncertainty in Coolant Mass Flow Rate

The uncertainty in coolant mass flow rate is calculated using Equation C.2. As published by the manufacturer, the volumetric mass flow rate meter has an uncertainty of 0.5%. This along with the uncertainty in the number of pulses is used to find the uncertainty in coolant mass flow rate of 0.7%.

$$\frac{W_{\dot{m}_c}}{\dot{m}_c} = \left[\left(\frac{W_{\rho_{c,out}}}{\rho_{c,out}} \right)^2 + \left(\frac{W_{Rc}}{Rc} \right)^2 + (0.5\%)^2 \right]^{1/2} \quad \text{(C.2)}$$

Uncertainty in V_{max}

Equation C.3 was used to determine the propagated uncertainty for $V_{max.}$ The frontal velocity was measured directly using an constant temperature thermal anemometer with a calibrated uncertainty of 1%. The uncertainty was found to be approximately 10% with an uncertainty in A_{fr} of 1.66% and A_{min} of 2.78%.

$$\frac{W_{V_{max}}}{V_{max}} = \left[\left(\frac{W_{V_{air}}}{V_{air}} \right)^2 + \left(\frac{W_{A_{fr}}}{A_{fr}} \right)^2 + \left(\frac{W_{A_{min}}}{A_{min}} \right)^2 + \left(\frac{W_{\rho_{air,in}}}{\rho_{air,in}} \right)^2 + \left(\frac{W_{\rho_{air}}}{\rho_{air}} \right)^2 \right]^{1/2} \quad \text{(C.3)}$$

Uncertainty in Air-Side Reynolds Number

The uncertainty in air-side Reynolds number is based on collar diameter and calculated using Equation C.4. The uncertainty in collar diameter and the air properties are negligible compared to the error in $V_{max,}$ therefore the uncertainty Reynolds number is also approximately 10%.

$$\frac{W_{Re_{Dcoll}}}{Re_{Dcoll}} = \left[\left(\frac{W_{G_{air}}}{G_{air}} \right)^2 + \left(\frac{W_{D_{coll}}}{D_{coll}} \right)^2 + \left(\frac{W_{\mu_{air}}}{\mu_{air}} \right)^2 \right]^{1/2} \quad \text{(C.4)}$$

Uncertainty in Air-Side Friction Factor

The uncertainty in air-side friction factor is determined by Equation C.5. Since the uncertainty in air density is small compared to that of $V_{max,}$ the uncertainty in mass velocity is also found to be approximately 10%. With an uncertainty in A_{min} of 2.78% and A_{tot} of 1.68% the uncertainty in air-side friction factor is determined to be 20.3%.

$$\frac{W_f}{f} = \left[\left(\frac{W_{\Delta P_{HX}}}{\Delta P_{HX}} \right)^2 + \left(2\frac{W_{G_{air}}}{G_{air}} \right)^2 + \left(\frac{W_{\rho_{air}}}{\rho_{air}} \right)^2 + \left(\frac{W_{A_{min}}}{A_{min}} \right)^2 + \left(\frac{W_{A_{tot}}}{A_{tot}} \right)^2 \right]^{1/2} \quad \text{(C.5)}$$

Uncertainty in Air-Side Sensible Heat Transfer Coefficient

The uncertainty in air-side sensible heat transfer coefficient is calculated using Equation C.6. An uncertainty in coolant-side sensible heat transfer coefficient h_i of 10%

is used based on the Handbook of Single-Phase Convective Heat Transfer [27]. The uncertainty in air-side sensible heat transfer coefficient is determined to be 11%.

$$\frac{W_h}{h} = \left[\begin{array}{l} \left(\frac{W_{T_{air,in}}}{T_{air,in}}\right)^2 + \left(\frac{W_{T_{air,out}}}{T_{air,out}}\right)^2 + \left(\frac{W_{\dot{m}_{air}}}{\dot{m}_{air}}\right)^2 + \left(\frac{W_{A_f}}{A_f}\right)^2 + \left(\frac{W_{A_P}}{A_P}\right)^2 + \\ \left(\frac{W_{T_{dp,in}}}{T_{dp,in}}\right)^2 + \left(\frac{W_{T_{dp,ou}}}{T_{dp,out}}\right)^2 + \left(\frac{W_{T_{c,in}}}{T_{c,in}}\right)^2 + \left(\frac{W_{T_{c,out}}}{T_{c,out}}\right)^2 + \left(\frac{W_{\dot{m}_c}}{\dot{m}_c}\right)^2 \end{array} \right]^{1/2} \quad \text{(C.6)}$$

Uncertainty in Air-Side Sensible Nusselt Number

The uncertainty in air-side sensible Nusselt number is calculated using Equation C.7. The uncertainty in collar diameter and the thermal conductivity of air are negligible compared to the error in air-side heat transfer coefficient, therefore the uncertainty Nusselt number is also approximately 11%.

$$\frac{W_{Nu_{Dcoll}}}{Nu_{Dcoll}} = \left[\left(\frac{W_h}{h}\right)^2 + \left(\frac{W_{D_{coll}}}{D_{coll}}\right)^2 + \left(\frac{W_{\kappa_{air}}}{\kappa_{air}}\right)^2 \right]^{1/2} \quad \text{(C.7)}$$

Uncertainty in Sensible *j* factor

The only significant contributions to the j factor uncertainty are from the mass velocity and the air-side heat transfer coefficient *h*. Since the uncertainty in air properties are small, the uncertainty in mass velocity is found to be approximately the same as V_{max} or 10%. The uncertainty in sensible j factor is calculated using Equation C.8 and determined to be 11.9%.

$$\frac{W_j}{j} = \left[\left(\frac{W_h}{h} \right)^2 + \left(\frac{W_{G_{air}}}{G_{air}} \right)^2 + \left(\frac{W_{C_{P,air}}}{C_{P,air}} \right)^2 + \left(\frac{W_{\mathrm{Pr}}}{\mathrm{Pr}} \right)^2 \right]^{1/2} \qquad \text{(C.8)}$$

Uncertainty in Measured Condensate Retention

The uncertainty in condensate retention measurements was hard to calculate since the uncertainties in the electronic balance are negligible to other sources of error. The values for the mass of retained condensate determined from the real-time experiments agreed within 15% of the measurement that were obtained from removal of the heat exchanger from the test section after prolonged operation under condensing conditions. While removing the heat exchanger from the test section spilling of condensate and evaporation may occur. Furthermore, during real-time condensate retention experiments the heat exchangers are exposed to a frontal air velocity, which will introduce friction between the heat exchanger and the test section wall, resulting in possible error in the electronic balance reading.

Table C.1 Uncertainties in measured parameters

Measured Parameter	Uncertainty
ΔP_{HX}	±0.124 Pa
$T_{air, in}$	±0.3°C
$T_{air,out}$	±0.3°C
$T_{c,in}$	±0.3°C
$T_{c, out}$	±0.3°C
$T_{dp, in}$	±0.2°C
$T_{dp, out}$	±0.2°C
Pulses	±0.5%
V_{air}	±1%

Table C.2 Uncertainties in reduced parameters

Reduced Parameter	Uncertainty
$\dot{m}_c$	0.7%
V_{max}	10%
Re_{Dcoil}	10%
f	20.3%
h	11%
Nu_{Dcoil}	11%
j	11.9%

Appendix D – Condensate Retention Model

Table D.1 shows the equation worksheet that was used to calculate the maximum droplet diameter which was determined from the balance between gravitional, surface tension, and air-flow forces given the air flow rate and the advancing and receding contact angles.

The equation worksheet that was used to calculate the mass of retained condensate for a plain-fin-and-tube heat exchanger is shown in Table D.2. The total mass of retained condensate may be estimated by summing the mass of condensate contributed by droplets with the contribution by fin-tube bridges as shown in Equation D.1.

$$M = \frac{1}{3}A_T\rho\int_{0.2D_{max}}^{D_{max}}\overline{N}_{D,top}\forall_D dD + \frac{1}{3}A_T\rho\int_{0.2D_{max}}^{D_{max}}\overline{N}_{D,mid}\forall_D dD + \frac{1}{3}A_T\rho\int_{0.2D_{max}}^{D_{max}}\overline{N}_{D,bot}\forall_D dD$$
$$+\frac{1}{3}A_T\rho\int_{20\mu m}^{0.2D_{max}}\overline{N}_{D,top}\forall_D dD + \frac{1}{3}A_T\rho\int_{20\mu m}^{0.2D_{max}}\overline{N}_{D,mid}\forall_D dD + \frac{1}{3}A_T\rho\int_{20\mu m}^{0.2D_{max}}\overline{N}_{D,bot}\forall_D dD \qquad (D.1)$$
$$+\rho\forall_{bridge}N_{tr}N_f$$

The approach used to get $\overline{N}$ was similar to Graham [20]. Since a change in the droplet distribution was found at $0.2D_{max}$ and the heat exchanger fin was split up into top, middle, and bottom sections a total of six droplet distributions were found using a variable bin size of D±0.1D. In each of the three sections, a curve fit was drawn through the data of log ΔN versus log D to determine the droplet distributions. This results in a droplet distribution for each section of the form $\Delta N = B_1 D^{-z}$. The equation for $\overline{N}$ is obtained by dividing the droplet distribution ΔN by the bin size ΔD. The variable bin size used for this research was $\Delta D = 0.2D$. Each of the droplet distributions was used to calculate the mass of retained condensate for a third of the total fin area.

Table D.1 EES code for calculating the maximum droplet diameter

```
"Unknowns: V_air, Theta_A, Theta_R"
alpha=90*pi/180                          {radians, vertical fins}
S=0.072                                  {N/m  Gamma}
T_water=12
rho=DENSITY(Water,T=T_water,P=101.325)
rho_air=1.225                            {Kg/m^3}
g=9.81
x=0.00635                                {m}
Cd=1.22
nu_air=0.0000145                         {m^2/s}
Rex=V_air*x/nu_air

Theta_M=(Theta_R+Theta_A)/2              {degrees}
Theta_Rrad=Theta_R*pi/180                {radians}
Theta_Arad=Theta_A*pi/180                {radians}
Theta_Mrad=Theta_M*pi/180                {radians}

"Droplet Volume"
Vol_left=pi*D_max^3/24
Vol_top=2-3*cos(Theta_Mrad)+cos(Theta_Mrad)^3
Vol_bot=sin(Theta_Mrad)^3
Volume=Vol_left*Vol_top/Vol_bot/1000^3

height=D_max/2-D_max/2*cos(Theta_Mrad)
delta=5.48*x/Rex^0.5*1000
u=V_air*(2*height/(2*delta)-(height/(2*delta))^2)
Reb=u*delta/1000/nu_air

"Surface Tension"
Fsx=S * D_max/2 * (Fsx_top1/Fsx_bot1 + Fsx_top2/Fsx_bot2)
Fsx_top1=sin(Theta_Rrad)-sin(Theta_Arad-pi)
Fsx_bot1=(Theta_Rrad-Theta_Arad)/pi +1
Fsx_top2=sin(Theta_Rrad)-sin(Theta_A+pi)
Fsx_bot2=(Theta_Rrad-Theta_Arad)/pi -1

"Gravitational"
Fgx=rho_H2O*g*Volume*sin(alpha)*1000

"Air-Flow"
Fdx=Cd/2*rho_air*u^2 * A_pr*1000
Apr_top1=(D_max/1000)^2*Theta_Mrad
Apr_bot1=4
Apr_top2=(D_max/1000)^2*cos(Theta_Mrad)*sin(Theta_Mrad)
Apr_bot2=4
A_pr=Apr_top1/Apr_bot1-Apr_top2/Apr_bot2

0=Fsx-Fgx-Fdx
```

Table D.2 EES code for calculating the total mass of condensate

```
"Unknowns: fpi, D_mm, exp, mass_drops, Theta_R, Theta_A, PercentCoverage"
"Geometry and Properties"
Hf=8*Convert(in,m)                                  {Height of fin, m}
W=12*Convert(in,m)                                  {Width of HX, m}
Lf=1.737*Convert(in,m)                              {Length of Fin, m}
L_t=W*Nt                                            {Tube Length, m}
D_coll=(0.405)*Convert(in,m)                        {Outside diameter of tube, m}
Nf=fpi*12                                           {Number of Fins given fpi}
Nfs=Nf*2-1                                          {Number of Fin Surfaces}
Nt=16                                               {Number of Tubes}
delta=.0045*Convert(in,m)                           {Fin Thickness, m}
Afs=(Hf*Lf)-(Nt*(D_coll+2*delta)^2)*(pi/4)          {Area per fin surface, m^2}
Af=Nfs*Afs                                          {Total fin area, m^2}
Area_total=Af*100^2                                 {cm^2}
Theta_Arad=Theta_A*pi/180
Theta_Rrad=Theta_R*pi/180
Theta_Mrad=(Theta_Arad+Theta_Rrad)/2
fs=(1/fpi)*Convert(in,m) – delta                    {fin pitch/spacing}
gamma=(75.83 - 0.1477*T_water)/1000                 {N/m  Gamma}
T_water=12                                          {degrees C}
rho=DENSITY(Water,T=T_water,P=101.325)
g=9.81

"Condensate Droplets"
D_max=D_mm*1000                                     {microns}
D_min=0.2*D_max                                     {microns}
top=PercentCoverage/100*10000^2                     {micron^2 covered per cm^2}
bottom=pi/4*(integral(D^(2+exp),D,D_min,D_max))
C=top/bottom
vol_PerSqCm=C*integral(D^(exp)*vol,D,D_min,D_max)
vol=pi*D^3/24*((2-3*cos(Theta_Mrad)+cos(Theta_Mrad)^3)/sin(Theta_Mrad)^3)    {micron^3}
vol_total=Area_total/3*vol_PerSqCm
mass_drops=vol_total/1000000^3*rho*1000             {g}

"Fin-tube bridges"
N=Nt*Nf/3
rho*g*V=2*gamma*fs*cos(Theta_Rrad)+2*gamma*l*cos(pi-Theta_Arad)
V=l*Lmax*fs+l*A2-A1*fs
A1=pi*R1^2*(2*(pi/2-Theta_Rrad)/360)-l/2*(R1^2-(l/2)^2)^.5
R1=D_coll/2
l=2*R1*sin(pi/2-Theta_Rrad)
A2=if(Theta_Arad,pi/2,A2_1,0,A2_2)
A2_1=pi*R2^2*(2*(Theta_Arad-pi/2)/2*pi)+fs/2*(R2^2-(fs/2)^2)^.5
A2_2=pi*R2^2*(2*(Theta_Arad-pi/2)/2*pi)-fs/2*(R2^2-(fs/2)^2)^.5
R2=fs/2/sin(Theta_Arad-pi/2)
V_mm=V*1000*1000*1000
mass_bridges=rho*V*N*1000

"Total mass of condensate"
mass_total=mass_drops + mass_bridges
```

References

[1] Bettanini, E., 1970, "Simultaneous Heat and Mass Transfer on a Vertical Surface," *International Institute of Refrigeration Bulletin*, Vol. 70, pp. 309-317.

[2] Guillory, J. L., and McQuiston, F. C., 1973, "An Experimental Investigation of Air Dehumidification in a Parallel Plate Heat Exchanger," *ASHRAE Transactions*, Vol. 79(2), pp. 146-151.

[3] McQuiston, F. C., 1976, "Heat, Mass, and Momentum Transfer in a Parallel Plate Dehumidifying Exchanger," *ASHRAE Transactions*, Vol. 82(2), pp. 87-107.

[4] Tree, D., and Helmer, W., 1976, "Experimental Heat and Mass Transfer Data for Condensing Flow in a Parallel Plate Heat Exchanger," *ASHRAE Transactions*, Vol. 82(1), pp. 289-299.

[5] McQuiston, F. C., 1978, "Heat, Mass and Momentum Transfer Data for Five Plate-Fin-Tube Heat Transfer Surfaces," *ASHRAE Transactions*, Vol. 84(1), pp. 266-293.

[6] McQuiston, F. C., 1978, "Correlation of Heat, Mass, and Momentum Transport Coefficients for Plate-Fin-Tube Heat Transfer Surfaces with Staggered Tubes," *ASHRAE Transactions*, Vol. 84(1), pp. 294-308.

[7] Seshimo, Y., Ogawa, K., Marumoto, K., and Fujii M., 1989, "Heat and Mass Transfer Performance on Plate Fin and Tube Heat Exchangers with Dehumidification," *Heat Transfer-Japanese Research*, Vol. 18(5), pp. 79-84.

[8] Wang, C. C., Hsieh, Y. C., and Lin, Y, T., 1997, "Performance of Plate Finned Tube Heat Exchangers Under Dehumidifying Conditions," *Journal of Heat Transfer*, Vol. 119, pp. 109-107.

[9] Korte, C. M., and Jacobi, A. M., 1997, "Condensate Retention and Shedding Effects on Air-Side Heat Exchanger Performance," ACRC-TR132, University of Illinois at Urbana-Champaign, IL.

[10] Chuah, Y. K., Hung, C., C., and Tseng, P. C., 1998, "Experiments on the Dehumidification Performance of a Finned Tube Heat Exchanger," *HVAC&R Research*, Vol. 4, pp. 167-178.

[11] Ha, S., Kim, C., Ahn, S. and Dreitser, G. A., 1999, "Hydraulic Performance of Wet-Fin-And-Tube Heat Exchanger for Various Wettability Surfaces," *Compact Heat Exchangers and Enhancement Technology for the Process Industries,* pp. 463-470.

[12] Yoshii T., Yamamoto, M., and Otaki, T., 1973, "Effects of Dropwise Condensate on Wet Surface Heat Transfer of Air Cooling Coils," *Proc. 13th Int. Congress of Refrigeration*, pp 285-292.

[13] Mirth, D. R., and Ramadhyani, S., 1993, "Prediction of Cooling-Coil Performance Under Condensing Conditions," *International Journal of Heat and Fluid Flow*, Vol. 14, pp. 391-400.

[14] Mirth, D. R., and Ramadhyani, S., 1994, "Correlations for Predicting the Air-Side Nusselt Numbers and Friction Factors in Chilled-Water Cooling Coils," *Experimental Heat Transfer*, Vol. 7, pp. 143-162.

[15] Youn, B., Kil, Y. H., Park, H. Y., Yoo, K. C., and Kim, Y. S., 1998. "Experimental Study of Pressure Drop and Heat Transfer Characteristics of ϕ 10.07 Wave and Wave-Slit Fin-Tube Heat Exchangers with Wave Depth of 2 mm," *Proceedings of 11th International Heat Transfer Conference*, Vol. 6, pp. 333-338.

[16] Jacobi, A. M., and Goldschmidt, V. W., 1990, "Low Reynolds Number Heat and Mass Transfer Measurements of an Overall Counterflow, Baffled, Finned-Tube, Condensing Heat Exchanger," *International Journal of Heat and Mass Transfer*, Vol. 33, pp. 755-765.

[17] Johnson, R. E. Jr. and Dettre, R. H., 1969, "Wettability and Contact Angles," *Surface and Colloid Science*, Vol 2. pp. 85-153.

[18] ARI, 1981, *Standard for Forced-Circulation Air-Cooling and Air-Heating Coils*, ARI-410.

[19] Uv, E. H., and Sonju, O. K., 1992, "Heat Transfer Measurements of Circular Finned Tubes With and Without Partial Condensation," *Institute of Chemical Engineers Symposium Series No. 129*, Vol. 1, pp. 295-302.

[20] Graham, C., 1969, "The Limiting Heat Transfer Mechanisms of Dropwise Condensation," PhD thesis, Massachusetts Institute of Technology, MA.

[21] Jasper, J. J., 1972, "The Surface Tension of Pure Liquid Compounds," *J. Phys. Chem. Ref. Data,* Vol. 1, pp. 841-1010.

[22] Gnielinski, V., 1976, "New Equations for Heat and Mass Transfer in Turbulent Pipe and Channel Flow," *Int. Chem. Eng.*, Vol. 16, pp. 359-368.

[23] Hong, T. K., and Webb, R. L., 1996, "Calculation of Fin Efficiency for Wet and Dry Fins," *International Journal of HVAC & R Research*, Vol. 2, pp. 27-41.

[24] Schmidt, T. E., 1949, "Heat Transfer Calculations for Extended Surfaces," *Refrigerating Engineering*, Vol. 57, pp. 351-357.

[25] Fox, R. W., and McDonald, A. T., 1985, *Introduction to Fluid Mechanics*, John Wiley & Sons, New York, NY.

[26] Kline, S. J., and McClintock, F. A., 1953, "Describing Experimental Uncertainties in Single Sample Experiments," *Mechanical Engineering*, Vol. 75, pp. 3-8.

[27] Kakac, S., Shaw, R. K., and Aung, W., 1987, *Handbook of Single-Phase Convective Heat Transfer*, John Wiley & Sons, New York, NY.